PHYSICAL REVIEW B VOLUME 52, NUMBER 2 1 JULY 1995-II

Atomic-structure model of i-($Al_{0.570}Cu_{0.108}Li_{0.322}$)

Shi-Yue Qiu*
Department of Physics, Iowa State University, Ames, Iowa 50011

Marko Vukobrat Jarić
Department of Physics, Texas A&M University, College Station, Texas 77843
and Nikola Tesla University, Knin

(Received 21 June 1994; revised manuscript received 22 August 1994)

An atomic-structure model of quasicrystalline i-($Al_{0.570}Cu_{0.108}Li_{0.322}$) is presented and compared with models obtained earlier using different approaches. The quasicrystal, assumed quasiperiodic, is represented by a higher-dimensional crystal which is modeled directly in the hyperspace, unprejudiced by any tiling assumptions. The modeling follows a method which systematically enforces chemical (steric and stoichiometric) constraints directly in the hyperspace. A detailed comparison and examination of earlier models using this method reveals significant violations of the constraints, including some unphysically short interatomic separations.

I. INTRODUCTION

Since the discovery of quasicrystals in 1984,[1] many researchers have concentrated their effort on determining atomic structures of quasicrystals. Structure determination is a necessary step in understanding and explaining stability and other physical properties of quasicrystals. Significant progress in quasicrystal structure determination has been achieved in the last few years. Most advances have been accomplished for decagonal quasicrystals,[2] but significant progress has been made also in modeling icosahedral[3] and, to a lesser extent, octagonal[4] and dodecagonal[5] quasicrystals. Structural models for several quasicrystalline compounds appear to be excellent candidates for the final structure refinement. In addition to the proposals for models of specific quasicrystalline compounds, there are also beginning to emerge some general principles and methodology of quasiperiodic crystal modeling.[6–8] Conceptual frameworks used in modeling quasicrystal structures[9] range from the large unit cell[10,11] and crystal twinning models,[10] through the bond-orientationally ordered glass[12] and random tiling models,[8,13,14] to the quasiperiodic crystal models.[15–19] Although there are now well-established "quasicrystalline" materials belonging to each of these conceptual frameworks, the quasiperiodic crystal concept appears to be the most developed.

In this paper, we shall construct a quasiperiodic crystal structure model of i-($Al_{0.570}Cu_{0.108}Li_{0.322}$). Our goal is for the model to achieve a sufficiently good fit of the experimentally obtained diffraction data, so that it can be used as a starting point in the final structure refinement. Although the major effort in quasicrystal structure determination is currently focused on compounds with much more perfect quasiperiodic order, several groups attempted to construct quasiperiodic structure models of i-($Al_{0.570}Cu_{0.108}Li_{0.322}$).[20–25] We believe that the representation of i-($Al_{0.570}Cu_{0.108}Li_{0.322}$) by a quasiperiodic crystal should be useful even if it is only an idealization. Such a view is supported by several observations. The quasicrystal diffraction peaks can be indexed to within 10^{-3} Å^{-1} using an icosahedral reciprocal lattice, and the coherence length, measured by the inverse of the characteristic half-width of the diffraction peaks, is not too short, on the order of 1000 Å.[25] Moreover, the i-($Al_{0.570}Cu_{0.108}Li_{0.322}$) Patterson function[24–28] is extremely simple when viewed as quasiperiodic,[24–26] which would not be expected if quasiperiodicity were a bad assumption. Similarly, the reconstructed quasiperiodic density of i-($Al_{0.570}Cu_{0.108}Li_{0.322}$) is also very simple.[29–31]

Although, based on general arguments,[15–19] all current quasiperiodic models of i-($Al_{0.570}Cu_{0.108}Li_{0.322}$) can be represented as six-dimensional periodic crystals, some of them are constructed as quasiperiodic tiling models in real space,[20,21,23] while others result from a more[25] or less[22,24] direct six-dimensional modeling. By systematically enforcing steric and stoichiometric constraints directly in six dimensions, our six-dimensional i-($Al_{0.570}Cu_{0.108}Li_{0.322}$) structure model is developed unprejudiced by any tiling assumptions. It incorporates the information obtained from our previous solutions of the phase problem[29,30] and from the subsequent density reconstruction.[31] In order to determine the model parameters, we fit the x-ray- and neutron-diffraction data of Ref. 25, collected for a sample with determined overall density and stoichiometry.[32] Having a well-characterized sample is essential to our approach in which density and stoichiometry are used as *a priori* constraints.

The result of our modeling is a quasiperiodic crystal structure with space group symmetry $P53m$.[33] It has a six-dimensional simple hypercubic lattice with three species of hyperatoms (three-dimensional volumes) per hypercubic unit cell. The three species are located at vertices (V), midedges (E), and body centers (B) of the hypercubic lattice, respectively. Each hyperatom is assumed to be parallel to the inner space and to have homogeneous chemical composition. The shapes of these hy-

0163-1829/95/52(2)/894(25)/$06.00

peratoms are shown in Fig. 1, and their chemical composition is listed in Table I. The other model parameters are the hyperatom Debye-Waller factors and an overall scale factor listed in Table II. In order to evaluate goodness of the fit obtained with our model, we calculated the standard crystallographic measures, the so-called R factors, listed in Table III. We obtained an excellent R factor $R_F=0.068$ for neutron-diffraction data and $R_F=0.123$ for x-ray data. Structural models with such residual factors are usually considered good starting points for the refinement of periodic crystal structures. We also list in Table III the deviations of the model's Al, Cu, and Li number densities from the experimentally determined ones.[32]

A comparison of our i-($Al_{0.570}Cu_{0.108}Li_{0.322}$) structure model with some earlier quasiperiodic structure models, also listed in Tables I–III, is complicated by several factors. Some of these models were fitted to data obtained on different samples. Moreover, the overall density[20] and stoichiometry[23,24] of these samples or values of some of the fitting parameters[21,23–25] were often not given. After making adjustments to deal with this, we find that although some of the models report somewhat lower R factors, our model is the only one that both satisfies steric constraints and produces atomic densities closest to the experimentally determined ones. Therefore we conclude that our model is an excellent starting point for the final structure refinement of the quasiperiodic structure model of i-($Al_{0.570}Cu_{0.108}Li_{0.322}$).

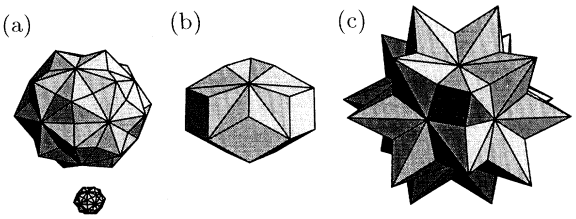

FIG. 1. Shapes of the (a) V, (b) E, and (c) B hyperatoms in our model of i-($Al_{0.570}Cu_{0.108}Li_{0.322}$) structure. The small volume in (a) shows the shape of the hole located at the center of the V hyperatom.

The rest of the paper is structured as follows. In Sec. II we state and justify our modeling assumptions and formulate a systematic approach for enforcing the chemical (stoichiometric and steric) constraints. In Sec. III we introduce a parametrization of hyperatom shapes and compositions for our modeling of i-($Al_{0.570}Cu_{0.108}Li_{0.322}$) hypercrystal and we present the results of the diffraction data fitting. Section IV is devoted to a discussion of the results: an evaluation of the results, their comparison with the earlier solutions of the phase problem, a summary of previous models, a comparison between the models, and a brief discussion of our model in the physical space. Conclusions of this paper are summarized in Sec. V. We also include four Appendixes in this paper. In

TABLE I. Optimal chemical compositions $p_{\mu i}$ of each hyperatom obtained in several models of i-($Al_{0.570}Cu_{0.108}Li_{0.322}$) for which we knew a hypercrystal description, as described in Sec. IV C. Rows are labeled by the source where the model was introduced. Only x-ray-diffraction data were used in the modeling, unless a second row is listed for the same source, in which case it refers to the neutron-diffraction data. For the sake of a comparison, results available from the embedding of R-($Al_{0.564}Cu_{0.116}Li_{0.320}$) in the hypercrystal and from a solution of the phase problem are listed in the first two rows. Numbers enclosed in parentheses are statistical errors in the last significant digits resulting from the fits. Question marks indicate that the uncertainty was not given in the reference. If the particular composition was fixed in the model, no uncertainty is listed.

Ref.	$p_{V,Al}$ (%)	$p_{V,Cu}$ (%)	$p_{V,Li}$ (%)	$p_{E,Al}$ (%)	$p_{E,Cu}$ (%)	$p_{E,Li}$ (%)	$p_{B,Al}$ (%)	$p_{B,Cu}$ (%)	$p_{B,Li}$ (%)
34[a]	54(1)	46(1)	0	88.6(6)	11.4(6)	0	21.4	0	78.6
30			0			0	25(4)	0	75(4)
20[b]	84.6	15.4	0	84.6	15.4	0	0	0	0
23	69(?)	22(?)	9(?)	75(?)	10(?)	15(?)	17(?)	0(?)	83(?)
24	72(?)	19(?)	9(?)	75(?)	11(?)	14(?)	15(?)	1(?)	84(?)
Appendix C	69(1)	31(1)	0	88.8(3)	11.2(3)	0	0	0	100
	81(6)	19(6)	0	85(2)	15(2)	0	0	0	100
22[c]	64(8)	36(8)	0	85(3)	15(3)	0	20.0	0	80.0
25	71.6(?)	28.4(?)	0	87.9(?)	12.1(?)	0	0	0	100
	71.6	28.4	0	87.9	12.1	0	0	0	100
Appendix D	76(1)	24(1)	0	86.6(3)	13.4(3)	0	0	0	100
	89(6)	11(6)	0	82(2)	18(2)	0	0	0	100
This paper	64(1)	36(1)	0	89.6(3)	10.4(3)	0	0	0	100
	77(6)	23(6)	0	86(2)	14(2)	0	0	0	100

[a]Percentages of the Al and Li at B are set equal the ratio of the number of embedded Al atoms (30) and the number of embedded Li atoms (110) to the total number of embedded atoms (140) at B (see Table IV below).

[b]Locations of Li were not given in this model.

[c]Both x-ray and neutron data were fitted simultaneously; Al and Li are not mixed, but belong to distinct hyperatoms associated with the body center.

TABLE II. Optimal Debye-Waller parameters B, $B^{\perp}$, and B^{x}, and the absolute scale s obtained in several models of $i(Al_{0.570}Cu_{0.108}Li_{0.322})$ for which we were able to extract their values as described in Sec. IV C. Pairs of rows, the first obtained for x-ray data and the second for neutron data, are labeled by the source where the model is presented. For the sake of a comparison, results available from solutions of the phase problem are listed in the first three rows. DW parameters are listed in the units of 10^{-2} Å^2 for B and Å^2 for B^{x} and $B^{\perp}$. The absolute scale s is listed in the units of $10^{-2}e/$Å^3 for x rays and 10^{-8} Å^{-2} for neutrons.

Ref.	B_V	B_{El}	B_{Et}	B_B	B_E^x	$B_V^{\perp}$	$B_{El}^{\perp}$	$B_{Et}^{\perp}$	$B_B^{\perp}$	s
29[a]	1.24(2)	1.24(2)	1.24(2)	1.24(2)	0	0.018(1)	0.018(1)	0.018(1)	0.018(1)	1.771(1)
	1.20(3)	1.20(3)	1.20(3)	1.20(3)	0	0.39(7)	0.39(7)	0.39(7)	0.39(7)	7.4(1)
30[b]	1.1(1)	1.3(2)	1.17(9)	0.8(5)	0.05(3)	<4.11(3)	<1.16(7) >0.2(2)	<4.12(2)	<4.12(2)	7.1(5)
Appendix C	1.45(6)	1.43(7)	1.15(4)	0.8(3)	−0.03(2)	0.00(4)	0.08(5)	0.21(5)	1.1(7)	1.81(2)
	1.4(1)	1.9(2)	1.26(8)	1.1(2)	0.0(2)	0.0(3)	0.0(3)	0.9(2)	0.9(8)	7.4(2)
22[c,d]	1.3(1)	1.14(6)	1.14(6)	1.6(2) 4(1)	0	0	0	0	0	
25,52[c]	1.41(4)	1.42(3)	1.42(3)	1.6(?)	0	0	0	0	0	1.7(?)
	1.30(6)	1.21(4)	1.21(4)	1.6(?)	0	0	0	0	0	7.8(?)
Appendix D	1.19(5)	1.41(6)	1.06(4)	2.2(3)	−0.040(1)	0.00(4)	0.12(4)	0.61(5)	0.1(3)	1.64(1)
	1.3(1)	1.9(2)	1.10(8)	1.3(2)	0.0(1)	0.0(3)	0.0(3)	1.1(2)	1.6(8)	6.8(2)
This paper	1.36(6)	1.32(7)	1.17(4)	1.5(2)	0.012(3)	0.41(7)	0.08(4)	0.00(5)	0.0(3)	1.69(1)
	1.2(1)	2.0(3)	1.10(8)	1.2(2)	−0.004(3)	0.3(4)	0.0(2)	0.0(1)	3(1)	7.2(2)

[a]Only the overall, spherical B and $B^{\perp}$ parameters are available.
[b]Only parameters for the neutron data are available.
[c]All Debye-Waller parameters were assumed to be spherical, $B_{El}=B_{Et}$.

TABLE III. Comparison between different models. For each model, the difference between the model and the experimental number densities of i-$(Al_{0.570}Cu_{0.108}Li_{0.322})$, Δn_i, is listed in the first three columns for the three chemical species i = Al, Cu, and Li. An overall measure of these differences, Δn, is given in the fourth column. Each row is labeled by the source of the model. Only x-ray-diffraction data were used in the modeling, unless a second row is listed for the same source, in which case it refers to the neutron-diffraction data. For comparison, the last row gives uncertainties in experimental determination of these densities. Note that we adjusted for differences in the lattice constants of i-$(Al_{0.570}Cu_{0.108}Li_{0.322})$ and the samples for which the models were developed by a uniform expansion or compression of the model. The frequency (per atom) of unphysically short interatomic distances occurring in the model is given in the fifth column. The sixth and seventh columns give the R factors and the numbers of the fitted independent peaks as found in the original papers. The remaining three columns list reduced χ^2 and two other common crystallographic measures for the goodness of the fit.

Ref.	Δn_{Al} (%)	Δn_{Cu} (%)	Δn_{Li} (%)	Δn (%)	n_{short} (%)	R_F (%)	N	χ_ν^2	R_{F^2} (%)	WR (%)
20[a]	16.8	11.9	24.2	31.8		10	20			
23,24[b]	8.4	−4.9	−4.1	10.6	0	7.0	37			
Appendix C	14.3	14.3	−24.5	31.8	0	13.8	56	31.5	14.0	25.4
						9.1	40	3.7	12.8	14.8
22	−3.6	7.5	0.8	8.4	4.2	7.6	56			
						8.5	40			
21[c]	−14.8	−14.8	−0.7	20.9	0	16	56			
						13	40			
25,52	−0.4	−0.9	−9.4	9.5	≈0.2	8	56	24	8	17
						8	40	4	11	14
Appendix D	−4.3	−4.3	−1.1	6.2	0	9.0	56	16.0	9.2	18.1
						7.5	40	3.2	9.7	13.8
This paper	−3.4	−3.4	−1.1	4.9	0	12.3	56	28.7	10.3	24.3
						6.8	40	2.4	8.7	12.0
Expt. (Ref. 32)	±1.5	±3.1	±3.4	4.8	0					

[a]Locations of Li were not given in this model, and so we determine Δn_{Li} using stoichiometry of the modeled sample.
[b]The results for the two models and samples are identical, but the additional 60 peaks measured in Ref. 24 cannot be fitted with either of the two models.
[c]We assumed that Al/Cu stoichiometry is the same in the model as it is in the sample.

Appendix A we summarize general results for calculating structure factors of a quasiperiodic crystal starting from the structure of its higher-dimensional crystal (hypercrystal) representation and we set most of the notation used in the paper. Readers, particularly those not very fluent with the hypercrystal approach to quasicrystals, are urged to read this appendix before proceeding to Sec. II. The relationship between quasiperiodic crystals and their periodic approximants is discussed in Appendix B from the point of view of hypercrystals. An Ammann tiling model of i-($Al_{0.570}Cu_{0.108}Li_{0.322}$) is formulated and results summarized in Appendix C. Another structure model of i-($Al_{0.570}Cu_{0.108}Li_{0.322}$) is analyzed in Appendix D.

II. CONSTRAINTS AND ASSUMPTIONS

In this section we shall introduce and justify several general assumptions that will be made in our modeling of the i-($Al_{0.570}Cu_{0.108}Li_{0.322}$) structure. Furthermore, we shall analyze and implement constraints imposed on our modeling by experimental observations. These assumptions and constraints will be based on experimental observations of i-($Al_{0.570}Cu_{0.108}Li_{0.322}$) (Refs. 25,32) and its related crystal structure R-($Al_{0.564}Cu_{0.116}Li_{0.320}$) (Ref. 34) and on reconstructed Patterson functions[24–28] and densities[29–31] for x-ray and neutron scattering. Since we are interested here in obtaining a good structural model of i-($Al_{0.570}Cu_{0.108}Li_{0.322}$) which is to serve as a starting point for a future refinement, it is expected that some of the simplifying assumptions that we shall make will be abandoned at the time of the refinement. We have relegated many of the technical definitions to Appendix A, and the reader unfamiliar with Refs. 29, 35, 36, and 39 is advised to check there if a term is not defined on its introduction.

Based on the observed positions of the diffraction peaks, our fundamental assumption is that the i-($Al_{0.570}Cu_{0.108}Li_{0.322}$) structure is quasiperiodic and can be described as a cut through a six-dimensional periodic hypercubic crystal with the lattice constant $\bar{a}=7.15$ Å.[25] We shall adopt the six-dimensional description in which the Cartesian basis $\bar{\mathbf{e}}_j$, $j=1,\ldots,6$, of the six-dimensional space is along the six orthogonal generators of the hypercubic lattice and its projections on the physical and inner space, $\bar{\mathbf{e}}_j \equiv (1/\sqrt{2})(\hat{\mathbf{e}}_j, \hat{\mathbf{e}}_j^{\perp})$, are along the six fivefold rotation axes of the icosahedral group. Whenever necessary, we shall use the specific coordinate systems and indexing described in Refs. 35,36. We shall assume that i-($Al_{0.570}Cu_{0.108}Li_{0.322}$) has $P53m$ space group symmetry[33] and that the embedding of the i-($Al_{0.570}Cu_{0.108}Li_{0.322}$) atoms into the hypercrystal results in three types of hyperatoms which are centered on vertices, edge centers, and body centers of the hyperlattice. These hyperatoms are assumed to be flat with uniform chemical compositions. The V and E hyperatoms may have different compositions, but are both assumed chemically disordered, partially occupied by Al and Cu. The B hyperatom is assumed to be composed exclusively of Li.

Our model will be constrained to reproduce the overall density and stoichiometry of the sample (within the experimental accuracy) and to respect the steric constraints, i.e., the minimal interatomic distances. We shall determine the model parameters in the next section by optimizing the differences between the predicted x-ray- or neutron-diffraction intensities and these observed in Ref. 25. This data set was collected using a sample with specified density and stoichiometry[32] that will be enforced in our model by fixing the volumes of the hyperatoms to $v_V^{\perp}+6v_E^{\perp}=5.48(7)\times10^3$ Å^3 and $v_B^{\perp}=2.60(5)\times10^3$ Å^3. We shall also strictly enforce the steric constraints by means of the restrictions they impose on hyperatom shapes. Thus the hyperatom shapes will be limited to the interior of certain "outer bounds" shown in Figs. 2(a) and 2(d), and they will not be allowed to have any overlaps when placed at the locations shown in Figs. 3(a)–3(f).

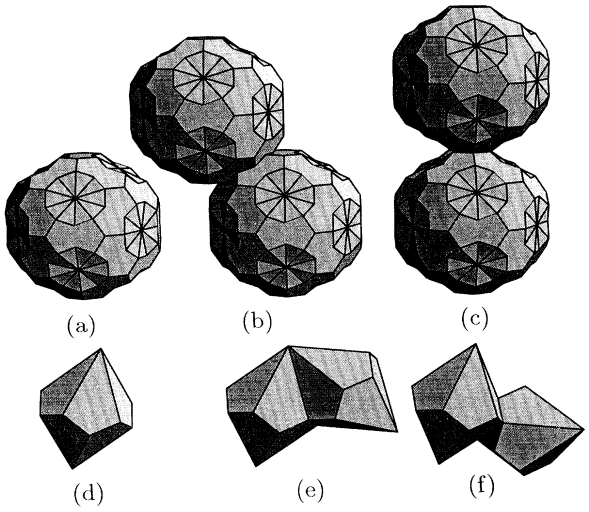

FIG. 2. Outer bounds for the (a) V or B and (d) E hyperatoms, resulting from their respective first [(b), (e)] and second [(c), (f)] second nonoverlap shells.

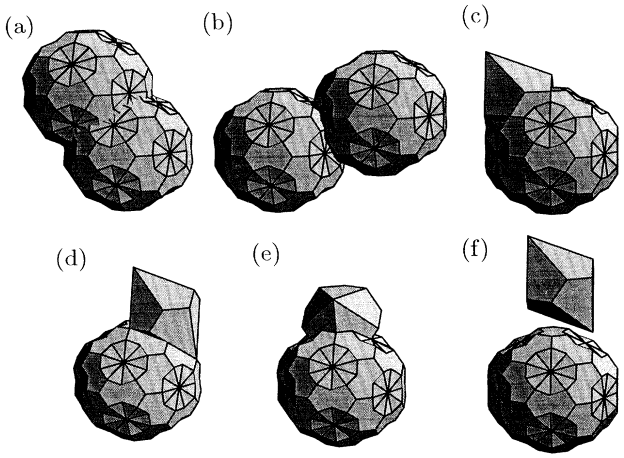

FIG. 3. Relative positions and orientations of the outer bounds in the first [(a), (c), (e)], and second [(b), (d), (f)], B-V [(a), (b)], B-E [(c), (d)], and V-E [(e), (f)] nonoverlap shells.

A. Hyperatom positions and fluctuations

An analysis of the six-dimensional Patterson functions[24,26] and reconstructed densities[29–31] of i-$(Al_{0.570}Cu_{0.108}Li_{0.322})$ is consistent with the $P53m$ space group symmetry[33] of the hypercrystal and with the hyperatoms located at the vertex

$$\bar{\mathbf{r}}_V=(000000)\ , \tag{2.1}$$

six equivalent edge centers

$$\bar{\mathbf{r}}_{E_1}=\frac{\bar{a}}{2}(100000),\ldots,\bar{\mathbf{r}}_{E_6}=\frac{\bar{a}}{2}(000001),\ldots, \tag{2.2}$$

and at the body center

$$\bar{\mathbf{r}}_B=\frac{\bar{a}}{2}(111111) \tag{2.3}$$

of the unit hypercell.

These conclusions are reinforced by an analysis of the R-$(Al_{0.564}Cu_{0.116}Li_{0.320})$ structure, viewed as a rational approximant of i-$(Al_{0.570}Cu_{0.108}Li_{0.322})$. As shown in Ref. 29, a crystalline structure very close to R-$(Al_{0.564}Cu_{0.116}Li_{0.320})$ can be obtained in physical space by a linear distortion of the i-$(Al_{0.570}Cu_{0.108}Li_{0.322})$ hypercrystal. Conversely, as demonstrated in Appendix B, by inverting this linear distortion, R-$(Al_{0.564}Cu_{0.116}Li_{0.320})$ can be lifted into the hypercrystal unit cell to give a discrete set of pointlike atoms at the locations listed in Table IV and shown in Fig. 4. Since these pointlike atoms should be located within the three-dimensional hyperatoms, their location and chemical composition may provide useful information about the locations, compositions, and, to a lesser extent, shapes of the hyperatoms. As already noted,[22,25] we can see that all seven orbits of the R-$(Al_{0.564}Cu_{0.116}Li_{0.320})$ atoms can be grouped into three sets in the hypercrystal: one around a vertex, another around an edge center, and the last one around a body center of the hypercubic unit cell. This association with vertices, edge centers, and body centers would be exact if the small physical space components $\Delta\mathbf{r}_k$ listed in the table were exactly zero. Therefore, in order to relate the embedded R-$(Al_{0.564}Cu_{0.116}Li_{0.320})$ with the hyperatoms in the i-$(Al_{0.570}Cu_{0.108}Li_{0.322})$, atomic coordinates in R-$(Al_{0.564}Cu_{0.116}Li_{0.320})$ need to be adjusted by expanding the R-$(Al_{0.564}Cu_{0.116}Li_{0.320})$ unit cell by a factor of $L^{-1}=1.001$ (to adjust the lattice constant of the crystal to that of the hypercrystal) and by setting $\Delta\mathbf{r}_k=0$.[22] The last condition is consistent with the assumption that the hyperatoms are flat, i.e., $\mathbf{s}_\mu(\mathbf{r}^\perp)=0$. The shapes of the hyperatom domains $v_\mu^\perp$ must be also consistent with the embedding of the so-adjusted R-$(Al_{0.564}Cu_{0.116}Li_{0.320})$. That is, the embedded atoms must fall within the domains $v_\mu^\perp$, as shown in Fig. 4.

We shall assume that any disordering of the hyperatoms around their positions given by Eqs. (2.1)–(2.3) is Gaussian and independent of $\mathbf{r}^\perp$,[36]

$$\bar{\mathsf{B}}_\mu(\mathbf{r}^\perp)\equiv\bar{\mathsf{B}}_\mu,\quad \mu=V,E_j,B\ . \tag{2.4}$$

From the Y_h symmetry of the vertices and body centers and the D_{5d} symmetry of the edge centers, we can also determine the number of independent components of $\bar{\mathsf{B}}_\mu$ tensors at these sites. Only the two diagonal blocks B_μ and $\mathsf{B}_\mu^\perp$ are nonzero for the vertex and the body center, and they are scalars,

$$\mathsf{B}_V\equiv B_V\mathsf{I},\quad \mathsf{B}_V^\perp\equiv B_V^\perp\mathsf{I}^\perp \tag{2.5}$$

and

$$\mathsf{B}_B=B_B\mathsf{I},\quad \mathsf{B}_B^\perp\equiv B_B^\perp\mathsf{I}^\perp\ , \tag{2.6}$$

where B_V, $B_V^\perp$, B_B, and $B_B^\perp$ are positive parameters and I and $\mathsf{I}^\perp$ are the unit matrices. For the edge center hyperatom at $\frac{1}{2}\hat{\mathbf{e}}_j$, the diagonal blocks are

$$\mathsf{B}_{E_j}\equiv B_{El}\hat{\mathbf{e}}_j\hat{\mathbf{e}}_j+B_{Et}(\mathsf{I}-\hat{\mathbf{e}}_j\hat{\mathbf{e}}_j)\ , \tag{2.7}$$

$$\mathsf{B}_{E_j}^\perp\equiv B_{El}^\perp\hat{\mathbf{e}}_j^\perp\hat{\mathbf{e}}_j^\perp+B_{Et}^\perp(\mathsf{I}^\perp-\hat{\mathbf{e}}_j^\perp\hat{\mathbf{e}}_j^\perp)\ , \tag{2.8}$$

and the off-diagonal block is

TABLE IV. Embedding of the R-$(Al_{0.564}Cu_{0.116}Li_{0.320})$ atoms into the hypercrystal. The crystal orbit number k and its chemical composition, as given in Ref. 34, are listed in the first two columns. The next column identifies the hyperatom type with which the embedded atom is associated. Multiplicity (size of the orbit) of the embedded atoms with respect to the corresponding hyperatom site is listed in the next column. Physical and inner space distances of the embedded atoms from the center of the associated hyperatoms are listed in the fifth and sixth columns. The inner space distances for the idealized R-$(Al_{0.564}Cu_{0.116}Li_{0.320})$ structure, in which case all $|\Delta\mathbf{r}_k|=0$, are indicated in the parentheses (Ref. 22). The R-$(Al_{0.564}Cu_{0.116}Li_{0.320})$ crystal is uniformly expanded by the factor $L^{-1}=1.001$ giving the periodic lattice constant $a_p=13.916$ Å.

k	Al:Cu:Li	$\mu(k)$	Orbit	$\lvert\Delta\mathbf{r}_k\rvert$ (Å)	$\lvert\Delta\mathbf{r}_k^\perp\rvert$ (Å)
1	88.6:11.4:0	E	10	0.0163	2.5995(2.5973)
2	0:0:100	B	20	0.0898	6.3841(6.3623)
3	0:0:100	B	60	0.0654	8.2038(8.2138)
4	53.8:46.2:0	V	60	0.1714	5.2339(5.1948)
5	88.6:11.4:0	E	20	0.0462	4.5080(4.4989)
6	100:0:0	B	30	0.3295	10.942(11.020)
7	0:0:100	B	30	0.1022	3.6492(3.6733)

$$\mathsf{B}^{x}_{E_j} \equiv B^{x}_{El}\hat{\mathbf{e}}^{\perp}_{j}\hat{\mathbf{e}}_{j} , \tag{2.9}$$

where B_{El}, B_{Et}, $B^{\perp}_{El}$, and $B^{\perp}_{Et}$ are positive parameters and $(B^{x}_{El})^2 \leq B_{El}B^{\perp}_{El}$. Because of the overall icosahedral symmetry, these parameters are independent of j.

B. Hyperatom compositions and volumes

Although some of the inner space variation seen in the reconstructed Patterson[24,26] and density[29–31] functions may come from a compositional variation of hyperatoms rather than from their Gaussian disordering,[37] we shall assume that the chemical composition of the hyperatoms is homogeneous. In other words, we shall assume that

$$p_{\mu i}(\mathbf{r}^{\perp}) \equiv p_{\mu i}, \quad i = \text{Al, Cu, Li} , \tag{2.10}$$

and, as a consequence,

$$f_{\mu}(\mathbf{Q},\mathbf{r}^{\perp}) \equiv f_{\mu}(\mathbf{Q}) = \sum_{i} p_{\mu i} f_i(\mathbf{Q}) . \tag{2.11}$$

However, in order to partially compensate for this simplification and since i-($Al_{0.570}Cu_{0.108}Li_{0.322}$) could be chemically (Al/Cu) disordered like R-($Al_{0.564}Cu_{0.116}Li_{0.320}$), we shall also assume that hyperatoms are *a priori* chemically mixed and that $p_{\mu i}$ are only constrained by Eqs. (A4)–(A6), namely,

$$0 \leq p_{\mu i} \leq 1 , \tag{2.12}$$

$$\sum_{i} p_{\mu i} = 1 , \tag{2.13}$$

and

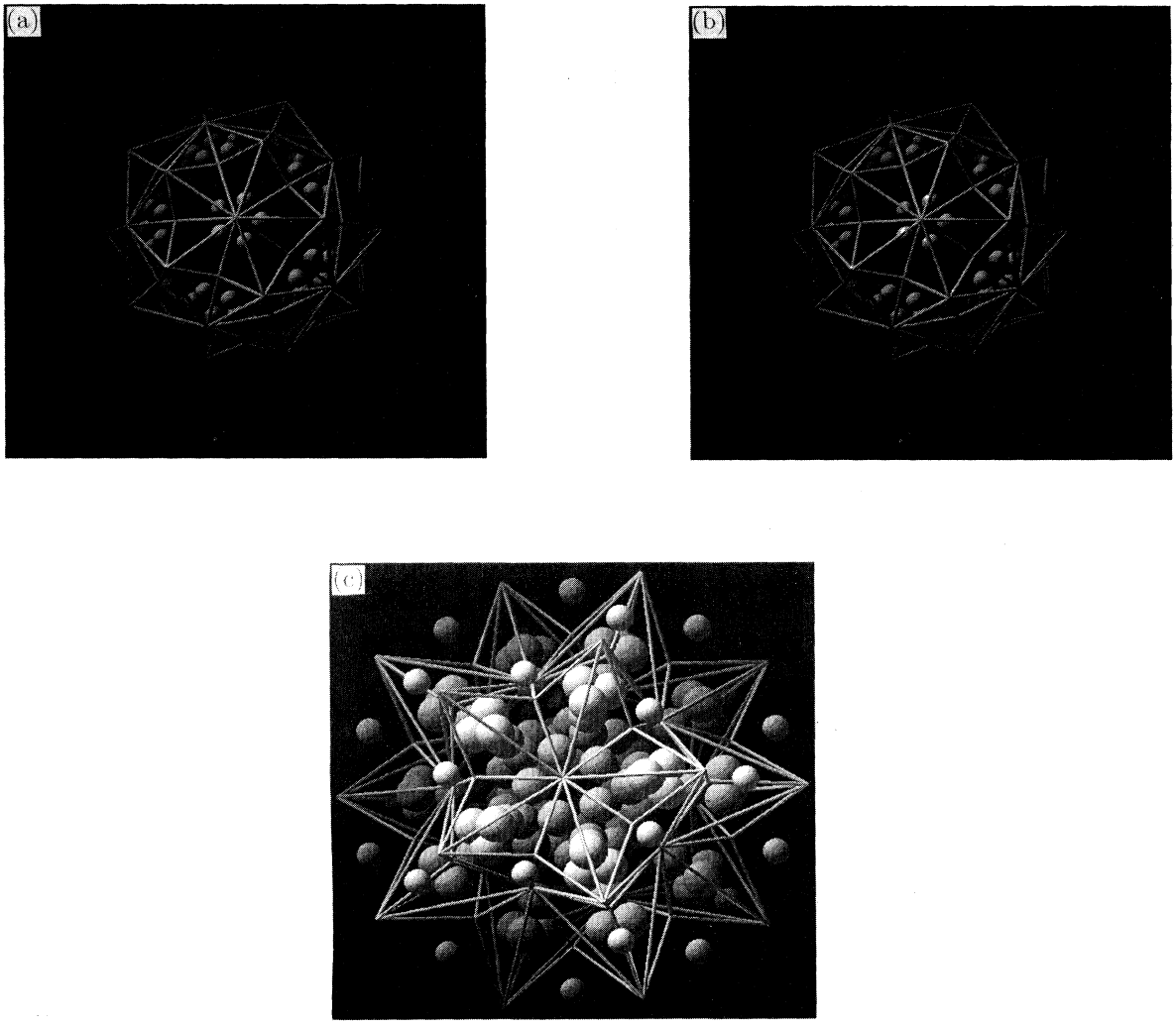

FIG. 4. Ideal inner space locations of the embedded R-($Al_{0.564}Cu_{0.116}Li_{0.320}$) atoms from Table IV. The clusters of embedded atoms are centered (a) at a vertex for orbit $K=4$, (b) at an edge center for orbits $k=1$ and 5, or (c) at a body center for orbits $k=2$, 3, 6, and 7. The spheres representing Li are the largest, with the size of spheres representing the other embedded atoms decreasing with the increase in Cu fraction. The correct site symmetries result from the five equivalent ways of embedding the crystal symmetry T_h into the hypercrystal symmetry Y_h. We also show the edges of the hyperatoms determined in our model.

$$\sum_{\mu} n_{\mu} p_{\mu i} = n_i \ . \tag{2.14}$$

Clearly, by symmetry, we must have $p_{E_j i} \equiv p_{Ei}$ and $n_{E_j} \equiv n_E$, independently of the edge direction. Further information about the chemical compositions $p_{\mu i}$ of the hyperatoms can be obtained from the *i*-($Al_{0.570}Cu_{0.108}Li_{0.322}$) density reconstruction.[29–31] We shall also use the established[38–44] structural similarity between crystalline *R*-($Al_{0.564}Cu_{0.116}Li_{0.320}$), whose structure is well known,[34] and quasicrystalline *i*-($Al_{0.570}Cu_{0.108}Li_{0.322}$).

The reconstructed six-dimensional *i*-($Al_{0.570}Cu_{0.108}Li_{0.322}$) density of x-ray scatters is significant only at vertices and edge centers, while the neutron scatterer density is appreciably positive at the vertices and edge centers, but considerably negative at the body centers.[29–31] This suggests that the *V* and *E* hyperatoms are chemically predominantly Al and Cu, while the *B* hyperatom is predominantly Li. Namely, Al and Cu are considerably stronger x-ray scatters than Li. They also have positive scattering lengths, while Li has a negative scattering length for neutrons. A more detailed quantitative analysis of the reconstructed densities at the vertex and edge center suggests that the Cu concentration is larger in the *V* than in the *E* hyperatom.

These conclusions are strengthened by results of the embedding of the crystal structure *R*-($Al_{0.564}Cu_{0.116}Li_{0.320}$) into the hypercrystal as shown in Fig. 4 and described above and in Appendix B. Indeed, we see from Table IV that the Cu-rich orbit ($Al_{0.538}Cu_{0.462}$, orbit No. 4) is the only orbit which maps into the vertex region, while the two Cu-poor orbits ($Al_{0.886}Cu_{0.114}$, orbits Nos. 1 and 5) are the only orbits that map into the edge centers. Similarly, all three Li orbits (Nos. 2, 3, and 7) map into the body center. In addition, the pure Al orbit No. 6 also maps into a body center.

Thus both the density analysis and the embedding of the *R* phase into the six-dimensional hypercrystal, described above, lead us to assume that the *V* and the *E* hyperatoms are each a mixture of Al and Cu only, with the *V* hyperatom being richer in Cu than the *E* hyperatom. Furthermore, we should also assume that there is a Li hyperatom and possibly an Al hyperatom at the body center. In order to simplify our analysis, we shall neglect here the body center Al hyperatom, which, based on the weak body center contribution to the x-ray Patterson[24–26] and density[29–31] functions, should have a smaller volume. However, this Al hyperatom should be included at the refinement stage. In summary, we shall assume

$$p_{V,\mathrm{Li}} = 0, \quad p_{V,\mathrm{Al}} + p_{V,\mathrm{Cu}} = 1 \ , \tag{2.15}$$

$$p_{E,\mathrm{Li}} = 0, \quad p_{E,\mathrm{Al}} + p_{E,\mathrm{Cu}} = 1 \ , \tag{2.16}$$

and

$$p_{B,\mathrm{Cu}} = p_{B,\mathrm{Al}} = 0, \quad p_{B,\mathrm{Li}} = 1 \ . \tag{2.17}$$

Using the measured mass density of $\rho = 2.46(1)$ g/cm^3 and the *i*-($Al_{0.570}Cu_{0.108}Li_{0.322}$) stoichiometry,[32] we can determine easily the number density n_i of each chemical species *i* from the equations

$$n_i = c_i \frac{\rho N_a}{\sum_j m_j c_j} \ , \tag{2.18}$$

where N_a is Avogadro's number, m_i is the atomic mass ($m_{\mathrm{Al}} = 26.982$ g, $m_{\mathrm{Cu}} = 63.546$ g, and $m_{\mathrm{Li}} = 6.941$ g), and c_i is the number fraction of *i*th species in *i*-($Al_{0.570}Cu_{0.108}Li_{0.322}$) [$c_{\mathrm{Al}} = 0.570(14)$, $c_{\mathrm{Cu}} = 0.108(4)$, and $c_{\mathrm{Li}} = 0.322(10)$]. This results in $n_{\mathrm{Al}} = 3.45(5) \times 10^{-2}$ Å^{-3}, $n_{\mathrm{Cu}} = 0.65(2) \times 10^{-2}$ Å^{-3}, and $n_{\mathrm{Li}} = 1.95(7) \times 10^{-2}$ Å^{-3}. Therefore, following Eqs. (2.13) and (2.14), we may immediately conclude that

$$n_T \equiv n_V + 6n_E + n_B = n_{\mathrm{Al}} + n_{\mathrm{Cu}} + n_{\mathrm{Li}} = 6.05(9) \times 10^{-2} \ \text{Å}^{-3} \ , \tag{2.19}$$

leading to the characteristic physical and inner space length scales $l = n_T^{-1/3} \approx 2.55$ Å and $l^{\perp} = n_T^{1/3} \bar{a}^{\,2} \approx 20.1$ Å, respectively. In addition, using our assumptions for $p_{\mu i}$ [Eqs. (2.15)–(2.17)], we also obtain

$$n_B = n_{\mathrm{Li}} = 1.95(7) \times 10^{-2} \ \text{Å}^{-3} \tag{2.20}$$

and

$$n_A \equiv n_V + 6n_E = n_{\mathrm{Al}} + n_{\mathrm{Cu}} = 4.10(7) \times 10^{-2} \ \text{Å}^{-3} \ . \tag{2.21}$$

Values of the hyperatom volumes will be constrained by the density and stoichiometry of *i*-($Al_{0.570}Cu_{0.108}Li_{0.322}$). Therefore it is more convenient to deal with the inner space volumes associated with each of the chemical species (by $v_i^{\perp} \equiv n_i \bar{v}$) than with the densities n_i themselves. Using the densities of Al, Cu, and Li, determined above, we find $v_{\mathrm{Al}}^{\perp} = 4.61(7) \times 10^3$ Å^3, $v_{\mathrm{Cu}}^{\perp} = 0.87(3) \times 10^3$ Å^3, and $v_{\mathrm{Li}}^{\perp} = 2.60(5) \times 10^3$ Å^3. This leads via Eq. (2.19) to the conclusion that the total inner space volume of the hyperatoms in the hypercubic unit cell, i.e., one at the vertex, plus six at the six mutually equivalent edge centers ($v_{E_j}^{\perp} \equiv v_E^{\perp}$), plus one at the body center, is

$$v_T^{\perp} \equiv v_V^{\perp} + 6v_E^{\perp} + v_B^{\perp} = v_{\mathrm{Al}}^{\perp} + v_{\mathrm{Cu}}^{\perp} + v_{\mathrm{Li}}^{\perp} = 8.08(9) \times 10^3 \ \text{Å}^3 \ . \tag{2.22}$$

Similarly, from Eq. (2.20), the volume of the hyperatom at the body center is

$$v_B^{\perp} = v_{\mathrm{Li}}^{\perp} = 2.60(5) \times 10^3 \ \text{Å}^3 \ , \tag{2.23}$$

while from Eq. (2.21) the sum of the volumes of the hyperatoms at the vertex and at the six edge centers is

$$v_A^{\perp} \equiv v_V^{\perp} + 6v_E^{\perp} = v_{\mathrm{Al}}^{\perp} + v_{\mathrm{Cu}}^{\perp} = 5.48(7) \times 10^3 \ \text{Å}^3 \ . \tag{2.24}$$

C. Steric constraints

In order to complete the characterization of our *i*-($Al_{0.570}Cu_{0.108}Li_{0.322}$) structure model, we shall fully describe the shapes (the boundaries) of the hyperatom domains $v_{\mu}^{\perp}$ in this section. We shall first specify the constraints and the assumptions which we impose. An analysis of *i*-($Al_{0.570}Cu_{0.108}Li_{0.322}$) x-ray and neutron Patterson[24–26] and density[29–31] functions strongly suggests

that we may assume that these hyperatoms are "flat," that is,

$$s_\mu(\mathbf{r}^\perp)\equiv 0, \quad \mu=V,E_j,B \ . \tag{2.25}$$

This conclusion is also supported by the embedding of R-($Al_{0.564}Cu_{0.116}Li_{0.320}$) in the hypercrystal described earlier. We note in Table IV that all Δr_k are small, suggesting that the corresponding hyperatoms are indeed flat.

The condition that no unphysically short interatomic distances are generated when the physical space cuts through the hypercrystal imposes strict geometrical (steric) constraints on the shape of hyperatomic domains. It follows from Eqs. (A11) and (2.25) that two hyperatoms, one at $\bar{r}_\mu$ and another one at $\bar{\mathbf{R}}+\bar{r}_\nu$, where $\bar{\mathbf{R}}$ is a hyperlattice translation, generate pairs of atoms in physical space separated by

$$\mathbf{r}_{\mu\nu}(\bar{\mathbf{R}})=\mathbf{R}+\mathbf{r}_\nu-\mathbf{r}_\mu \ , \tag{2.26}$$

if and only if the inner space domains of these two hyperatoms have a nonzero inner space volume overlap $v^\perp_{\mu\nu}(\bar{\mathbf{R}})$ defined in Eq. (A10). Therefore, if an interatomic distance $\mathbf{r}_{\mu\nu}(\bar{\mathbf{R}})$ is not allowed in the structure model of the quasiperiodic crystal, then the inner space overlap volume $v^\perp_{\mu\nu}(\bar{\mathbf{R}})$ of the corresponding hyperatoms must vanish. This imposes conditions on the modeling of the shapes of the hyperatom domains which we shall implement in the following fashion.

Let us denote by $r_{\mu\nu(\min)}$ the shortest physical distance allowed between the chemical species of the μth and νth hyperatom. Then we must make sure that the domain shapes $v^\perp_\mu$ and $v^\perp_\nu$ are such that the overlap $v^\perp_{\mu\nu}(\bar{\mathbf{R}})$ vanishes for all hyperlattice vectors $\bar{\mathbf{R}}$ for which the separation $\mathbf{r}_{\mu\nu}(\bar{\mathbf{R}})$ is smaller than $r_{\mu\nu(\min)}$. Formally, this condition is

$$v^\perp_{\mu(\mathbf{r}^\perp_\mu)} \cap v^\perp_{\nu(\mathbf{R}^\perp+\mathbf{r}^\perp_\nu)}=\emptyset$$

for all $\mu,\nu,\bar{\mathbf{R}}$

such that $|\mathbf{R}+\mathbf{r}_\nu-\mathbf{r}_\mu|<r_{\mu\nu(\min)}$. (2.27)

Therefore, given μ and ν, we select a hyperatom position $\bar{r}_\mu$ within the unit cell $\bar{v}$ of the hypercrystal. Next, we form a cylinder (tube) parallel to the inner space that intersects physical space on a sphere of diameter $r_{\mu\nu(\min)}$ centered at $\mathbf{r}_\mu$. The locations of the hyperatoms of type ν inside the cylinder project onto inner space and give a discrete set of isolated points $\{\mathbf{R}^\perp+\mathbf{r}^\perp_\nu\}$ that surround the projection $\mathbf{r}^\perp_\mu$ of the original site. This is a consequence of the general fact that an upper bound on the separation in physical space implies a lower bound on the separations in inner space. Then the hyperatom domains $v^\perp_\mu$ and $v^\perp_\nu$ must be chosen so that there is no overlap between the domain $v^\perp_\mu$ placed at $\mathbf{r}^\perp_\mu$ and $v^\perp_\nu$ placed at any of the projected locations $\mathbf{R}^\perp+\mathbf{r}^\perp_\nu$. Typically, the closer the location $\mathbf{R}^\perp+\mathbf{r}^\perp_\nu$ to a given $\mathbf{r}^\perp_\mu$, the more restrictive the nonoverlap constraint will be. Therefore we shall first classify the "neighbors" $\mathbf{R}^\perp+\mathbf{r}^\perp_\nu$ of $\mathbf{r}^\perp_\mu$ into "shells" according to their distance to $\mathbf{r}^\perp_\mu$. Alternatively, Voronoi polyhedra around the central site may be used to define the shells. Then we shall examine the nonoverlap constraint in that order (first shell, second shell, etc.). It is clear that going beyond a certain shell will produce no additional constraints so that only a finite number of hyperatom locations will need to be examined.

This test has to be carried out for all μ and ν, but it is useful to start with $\mu=\nu$ since in that case symmetry and the equivalence of $\mathbf{r}^\perp_\mu$ and $\mathbf{R}^\perp+\mathbf{r}^\perp_\mu$ can be used most efficiently to restrict the shape of $v^\perp_\mu$. In cases with a sufficiently high symmetry, this yields for a given μ an inner space (polyhedral) boundary, which we shall call "outer bound(ary)," within which the hyperatom shape $v^\perp_\mu$ must be contained in order for the steric constraints between all pairs of atoms of type μ to be satisfied. The condition Eq. (2.27) with $\mu\neq\nu$ can be used to further constrain the hyperatom shapes.

D. Outer bounds on hyperatom shapes

In order to apply constraint Eq. (2.27) to i-($Al_{0.570}Cu_{0.108}Li_{0.322}$) quasicrystal, it is first necessary to determine the shortest allowed interatomic distances $r_{\mu\nu(\min)}$. For example, to determine $r_{\mu\nu(\min)}$ we could use the appropriate atomic radii of the constituent elements. However, in the case of i-($Al_{0.570}Cu_{0.108}Li_{0.322}$) we also have the crystalline R-($Al_{0.564}Cu_{0.116}Li_{0.320}$), which has similar local atomic arrangements.[34] The shortest interatomic distances between the atoms were reported in Ref. 34 for each of the seven orbits listed in Table IV. After identifying Al and Cu, since they are not distinguished in our model of the i phase, we find that the shortest distances among Al/Cu and Li atoms are

$$r_{\mathrm{Al/Cu,Al/Cu}}=2.532 \text{ Å} \ , \tag{2.28}$$

$$r_{\mathrm{Li,Li}}=2.942 \text{ Å} \ , \tag{2.29}$$

$$r_{\mathrm{Al/Cu,Li}}=2.854 \text{ Å} \ . \tag{2.30}$$

These values are consistent with the atomic (metallic) radii of Al (1.432 Å), Cu (1.278 Å), and Li (1.562 Å) and their interatomic separations found in simple alloys.[45]

Since we assumed that the V and E hyperatoms are occupied by Al/Cu, while the B hyperatom is occupied by Li, we immediately obtain

$$r_{VV(\min)}=r_{EE(\min)}=r_{VE(\min)}\approx 2.532 \text{ Å} \ , \tag{2.31}$$

$$r_{BB(\min)}\approx 2.942 \text{ Å} \ , \tag{2.32}$$

$$r_{BV(\min)}=r_{BE(\min)}\approx 2.854 \text{ Å} \ . \tag{2.33}$$

These values, which are in agreement with several experimental results for i-($Al_{0.570}Cu_{0.108}Li_{0.322}$),[27,38–42] represent approximate bounds. For example, the embedding into the hypercrystal of the idealized R-($Al_{0.564}Cu_{0.116}Li_{0.320}$) leads to $r_{VE}\approx 2.528$ Å, which is smaller than $r_{VE(\min)}$ given in Eq. (2.31), but will be accepted in our model.

The minimal distances in physical space given in the above equations and the locations of the hyperatoms given in Eqs. (2.1)–(2.3) can be now used in the constraints expressed by Eq. (2.27). As described above, for

each μ we first construct the inner space shells of hyperatoms of each type ν whose domains are not allowed to overlap with the central μ domain. We found that it is sufficient to consider only the first two shells for each pair of hyperatom types, listed in Table V, since further shells do not effect any additional constraints. As an illustration, the first shell of V hyperatoms around a B hyperatom consists of 12 equivalent hyperatoms ($m_{BV}=12$) at the distance $r_{BV}^{\perp}=13.236$ Å along the 12 fivefold axes of the icosahedral symmetry of the body center site. A representative V hyperatom is located at $(\bar{a}/2)(1\bar{3}1111)$ relative to the B hyperatom. The corresponding physical space distance between them, $r_{BV}=1.931$ Å, is smaller than the minimal allowed distance $r_{BV(\min)}=2.854$ Å given in Eq. (2.33).

Since V and B hyperatoms have the identical Y_h symmetries and as seen in Table V the first two V-V shells are identical to the first two B-B shells, the outer bounds for the two types of hyperatoms are also identical. The resulting outer bound is shown in Fig. 2(a). It is easiest to construct it by starting from the second shell. The second shell consists of 30 hyperatoms at the distance of $2\eta\tau^3 a=22.519$ Å along the 30 twofold symmetry axes, where $a=\bar{a}/\sqrt{2}=5.056$ Å is a projection onto the inner space of the hyperlattice constant $\bar{a}$, $\tau\equiv(1+\sqrt{5})/2$ and $\eta=1/\sqrt{2+\tau}$. If we consider a second shell hyperatom along one of these 30 axes, we see that the resulting bounding surface should have D_{2h} symmetry centered at the point halfway along, and aligned with, this axis. For a simply connected domain, this forces the bounding surface to be the D_{2h} mirror plane perpendicular to the twofold axis. The 30 such planes, perpendicular to the 30 twofold directions of Y_h, close an outer bound, as can be seen in Fig. 2(c). It is a rhombic triacontahedron of edge τa and diameters of $2\tau^2 a=26.474$ Å, $2\sqrt{3}\eta\tau^2 a=24.106$ Å, and $2\eta\tau^3 a=22.518$ Å, along fivefold, threefold, and twofold axes, respectively.

The first V-V or B-B shell consists of 12 hyperatoms at the distance of $\tau^3 a=21.417$ Å along the 12 fivefold symmetry axes, as shown in Fig. 2(b). The bounding surface between the hyperatoms at the center and along one of these 12 axes must have D_{5d} symmetry aligned with this axis and centered halfway along it. Therefore, besides going through the center of D_{5d}, this bounding surface must also pass through the 5 twofold axes of D_{5d} and through the line along which the two triacontahedra intersect (puckered decagons in the figure). However, these conditions are insufficient to completely fix this surface. The simplest surface would consist of triangular elements connecting a puckered decagon to its center, as shown in the figure.[46]

An E hyperatom and its outer bound have D_{5d} symmetry. The outer bound on the E hyperatom shown in Fig. 2(d) is completely closed by the first E-E shell. As a consequence of the $P53m$ space group symmetry, a first shell E hyperatom is a mirror image of the central E hyperatom, as shown in Fig. 2(e). Therefore, if the E hyperatom is simply connected, the corresponding bounding surface must coincide with the mirror plane. Ten of these planes completely close the outer bound of the E hyperatom. The second E-E shell produces only overlaps along lines as shown in Fig. 2(f).

Further restrictions on the hyperatom shapes will come from the B-V, B-E, and V-E shells, that is, the case $\mu\neq\nu$ in Eq. (2.27). For all $\mu\neq\nu$ cases up to the second shell, we show in Fig. 3 relative positions and orientations of the outer bounds determined by the $\mu=\nu$ considerations. The first B-V shell hyperatoms are $\tau^2 a=13.237$ Å apart along fivefold axes, while the second B-V shell hyperatoms are $\sqrt{3}\eta\tau^3 a=19.501$ Å apart along threefold axes, as shown in Figs. 3(a) and 3(b). Both shells cause overlaps of the outer boundaries determined so far for B and V domains and will have to be considered in the modeling of V and B hyperatoms.

The first B-E shell hyperatoms are $\tau^3 a/2=10.708$ Å apart along the common fivefold axis, as shown in Fig. 3(c). Since the fivefold tip of the E outer bound coincides with the center of the B outer bound, it is clear that any B hyperatom will impose a truncation of the E outer boundary. The second B-E shell hyperatoms share a mirror plane. One fivefold vertex of the E outer bound coincides with a threefold vertex of the B outer boundary, while the other fivefold vertex of the E outer bound is $2\eta\tau^3 a=22.518$ Å away from the center of the B outer bound along a twofold axis, as shown in Fig. 3(d). Therefore there are nonzero overlaps between outer bounds in both B-E shells that must be considered in modeling B and E hyperatoms.

The first V-E shell hyperatoms also share a mirror plane. One fivefold vertex of the E outer bound is $\tau^2 a$ from the center of the V outer bound along a fivefold axis, while the other fivefold vertex is $\sqrt{3}\eta\tau^3 a$ from the center along a threefold axis, as shown in Fig. 3(e). This first V-E shell causes an overlap between the outer boundaries of V and E domains. The second V-E shell hypera-

TABLE V. First two shells of pairs of hyperatoms which would generate unphysically short interatomic distances in physical space if their hyperatom domains were to overlap. The first column indicates the hyperatom types in the pair. Columns 2–5 give, for each shell, number $m_{\mu\nu}$ of ν hyperatoms in the shell around a μ hyperatom (and vice versa), the six-dimensional separation $\bar{\mathbf{r}}_{\mu\nu}$ between the two representative hyperatoms, and its physical and inner space projections. The hypercrystal lattice constant is $\bar{a}=7.15$ Å.

μ-ν	$m_{\mu\nu}$-$m_{\nu\mu}$	$\bar{\mathbf{r}}_{\mu\nu}$ ($\bar{a}$)	$r_{\mu\nu}$ (Å)	$r_{\mu\nu}^{\perp}$ (Å)
B-V	12-12	$\frac{1}{2}(1\bar{3}1111)$	1.931	13.236
	20-20	$\frac{1}{2}(3\bar{3}11\bar{1}3)$	1.785	19.502
B-E	12-2	$\frac{1}{2}(1\bar{2}1111)$	0.597	10.708
	60-10	$\frac{1}{2}(1\bar{2}1\bar{1}\bar{1}3)$	2.399	14.544
B-B	12-12	$(1\bar{2}1111)$	1.194	21.417
	30-30	$(1\bar{2}1002)$	2.031	22.519
V-V	12-12	$(1\bar{2}1111)$	1.194	21.417
	30-30	$(1\bar{2}1002)$	2.031	22.519
V-E	60-10	$\frac{1}{2}(2\bar{1}00\bar{2}2)$	1.748	12.770
	60-10	$\frac{1}{2}(3\bar{4}0202)$	2.262	20.410
E-E	10-10	$\frac{1}{2}(2\bar{1}00\bar{1}2)$	1.015	11.259
	20-20	$\frac{1}{2}(0\bar{1}2\bar{2}\bar{1}2)$	1.193	13.236

toms again share a mirror plane. A fivefold vertex of the E outer bound is located exactly at the same point as in the first V-E shell, $\tau^2 a$ from the center of the V outer bound along a fivefold axis. However, as shown in Fig. 3(f), the E outer bound is oriented here like it is in the second B-E shell [Fig. 3(d)]. Since there is no overlap between the second shell V-E outer bounds, only the first shell overlaps need to be considered in modeling V and E hyperatoms.

III. PARAMETRIZATION AND FITTING

In this section we shall describe a parametrization of hyperatom shapes and show that the hyperatom volume constraints [Eqs. (2.23) and (2.24)] and the nonoverlap steric constraints [Eq. (2.27)] completely fix the parameters yielding the shapes shown in Fig. 1. Then we shall show that the Al concentration in the vertex hyperatom is the only parameter needed to specify the composition of the hyperatoms. Finally, we shall formulate our optimization procedure for fitting experimental diffraction data, present results of the optimization listed in Tables I–III, and quantify the goodness of the fit.

A. Hyperatom shape parametrization

There are several ways of parametrizing hyperatom shapes, depending on the assumptions that restrict the class of possible shapes. For example, as in the study of quasicrystal stability,[47] it can be assumed that the boundary of a hyperatom is described by a function $r^{\perp}=\psi_{\mu}(\hat{\mathbf{r}}^{\perp})$. This function would then be expanded in properly symmetrized spherical harmonics (Y_h harmonics for $\mu=V$ and B or D_{5d} harmonics for $\mu=E_j$), the sum truncated, and the expansion coefficients used as fitting parameters. However, an implementation of the constraints [Eq. (2.27)] would be highly nontrivial in this case. Moreover, if the domain $v_{\mu}^{\perp}$ happens to be polyhedral, as in the tiling models, it may be necessary to keep a large number of terms in the expansion. On the other hand, by using a sufficiently fine triangulation, any domain shape can be approximated with a polyhedron, reducing the constraints [Eq. (2.27)] to a system of linear inequalities. Therefore we shall assume here that we can model each $v_{\mu}^{\perp}$ by a polyhedron and we shall consider only the coarsest triangulation consistent with the constraints.

Since the inner space volume of the body center hyperatom, Eq. (2.23), is completely fixed by our earlier assumptions, Eq. (2.17), we found that it is easiest to first concentrate on the modeling of this hyperatom. Since the body center domain has the full icosahedral symmetry, it is sufficient to model only its generic element (fundamental region). The icosahedral symmetry operations will generate 120 replicas of this element to form the complete body center domain. This generic element is a cone bounded by three mirror planes which intersect along three neighboring twofold, threefold, and fivefold rotation axes of the icosahedral symmetry. We shall assume that $v_B^{\perp}$ is a solid object with only an external boundary. The coarsest triangulation of this boundary results from a single triangle per generic element. It can be parametrized with the radii along the twofold, threefold, and fivefold rotation axes, denoted $r_2^{\perp}$, $r_3^{\perp}$, and $r_5^{\perp}$, respectively. We shall vary these three radii to generate different shapes of the body center hyperatom. This parametrization includes an Ammann tiling model of i-($Al_{0.570}Cu_{0.108}Li_{0.322}$) further discussed in Appendix C. For more complicated domain shapes, which may be necessary in the refinement process, one can introduce more parameters associated with a finer triangulation.

It is not difficult to find a range of allowed variation of the radii $r_2^{\perp}$, $r_3^{\perp}$, and $r_5^{\perp}$ and a constraint that they must satisfy. Earlier consideration of the outer bound of the B hyperatom shown in Fig. 2(a) is sufficient to determine the upper bounds $r_5^{\perp}\le\tau^3 a/2=10.708$ Å, $r_3^{\perp}\le\sqrt{3}\eta\tau^2 a=12.053$ Å, and $r_2^{\perp}\le\eta\tau^3 a=11.259$ Å. No additional inequalities are needed to satisfy the B-B nonoverlap constraints. However, since the volume of the body center hyperatom is fixed by Eq. (2.23) to $v_B^{\perp}=2.60(5)\times10^3$ Å^3, it establishes an additional constraint which can be used to provide lower bounds on the radii and to eliminate one of them in favor of the other two. It is a matter of simple geometry to evaluate

$$v_B^{\perp}=120\left[\frac{1}{6}\frac{\eta}{\tau\sqrt{3}}\right]r_5^{\perp}r_3^{\perp}r_2^{\perp}\ . \tag{3.1}$$

Thus, by setting the right-hand side equal to $2.60(5)\times10^3$ Å^3, we obtain $r_5^{\perp}r_3^{\perp}r_2^{\perp}=0.69(1)\times10^3$ Å^3, allowing us to set a lower bound on each of the radii by taking the other two at their maximum values. This leads to $r_5^{\perp}\ge5.1(1)$ Å$\approx a=5.056$ Å, $r_3^{\perp}\ge5.8(1)$ Å$\approx2\sqrt{3}\eta\tau^{-1}a=5.690$ Å, and $r_2^{\perp}\ge5.4(1)$ Å$\approx2\eta a=5.316$ Å. Since the approximate values are within the experimental error bars, but considerably simplify further analysis, we shall use them below. The resulting value of $r_5^{\perp}r_3^{\perp}r_2^{\perp}$ is $\sqrt{3}\eta^2\tau^5 a^3=686$ Å^3, and the volume of the body center hyperatom,

$$v_B^{\perp}=2574\ \text{Å}^3\ , \tag{3.2}$$

agrees with experimental value $2.60(5)\times10^3$ Å^3 within the error bars. In summary, we shall restrict the radii $r_2^{\perp}$, $r_3^{\perp}$, and $r_5^{\perp}$ by the volume constraint

$$r_5^{\perp}r_3^{\perp}r_2^{\perp}=\sqrt{3}\eta^2\tau^5 a^3=686\ \text{Å}^3 \tag{3.3}$$

and limit them to the range

$$5.056\ \text{Å}=a\le r_5^{\perp}<\frac{\tau^3}{2}a=10.708\ \text{Å}\ , \tag{3.4}$$

$$5.690\ \text{Å}=2\sqrt{3}\eta\tau^{-1}a\le r_3^{\perp}\le\sqrt{3}\eta\tau^2 a=12.053\ \text{Å}\ , \tag{3.5}$$

$$5.316\ \text{Å}=2\eta a\le r_2^{\perp}\le\eta\tau^3 a=11.259\ \text{Å}\ . \tag{3.6}$$

For given values of $r_2^{\perp}$, $r_3^{\perp}$, and $r_5^{\perp}$ which satisfy the above conditions, the outer bounds of V and E hyperatoms shown in Figs. 2(a) and 2(b) are further restricted by the B-V and B-E constraints, respectively. However, we find that the total volume of the resulting V and E outer bounds remains too small for the condition $v_V^{\perp}+6v_E^{\perp}=5.48(7)\times10^3$ Å^3 given by Eq. (2.24) to be satisfied for any values of $r_2^{\perp}$, $r_3^{\perp}$, and $r_5^{\perp}$ that satisfy Eqs. (3.4)–(3.6). The maximal value

$$v_V^{\perp}+6v_E^{\perp}=5317\ \text{Å}^3\ , \tag{3.7}$$

only 3.0% short of the experimental value $5.48(7)\times10^3$ Å^3, is obtained for

$$r_{B5}^{\perp}=\frac{\tau^2}{2}a=6.618\ \text{Å}\ , \tag{3.8}$$

$$r_{B3}^{\perp}=\sqrt{3}\eta\tau^2 a=12.053\ \text{Å}\ , \tag{3.9}$$

$$r_{B2}^{\perp}=2\eta\tau a=8.602\ \text{Å}\ . \tag{3.10}$$

Therefore, for our best approximation, we should use these values for the B hyperatom, resulting in the shape shown in Fig. 1(c), while the V and E hyperatoms should fill what remains of their respective outer bounds.

The resulting V and E hyperatom shapes are shown in Figs. 1(a) and 1(b). The E hyperatom can be described by its edge lengths: The rhombus edge length of 5.056 Å (with the short rhombus diagonal of 5.316 Å) and the other two triangle edges of lengths 7.893 and 4.576 Å. It has D_{5d} symmetry and its volume is $V_E^{\perp}=694.3$ Å^3. Similarly to the B hyperatom, the V hyperatom has Y_h symmetry and can be described with three radii along the three symmetry axes

$$r_{V5}^{\perp}=\frac{\tau^2}{2}a=6.618\ \text{Å}\ , \tag{3.11}$$

$$r_{V3}^{\perp}=\sqrt{3}\eta\tau a=7.449\ \text{Å}\ , \tag{3.12}$$

$$r_{V2}^{\perp}=2\eta^3\tau^3 a=6.224\ \text{Å}\ . \tag{3.13}$$

Its volume is $v_{Vo}^{\perp}=1151$ Å^3. However, we shall modify this vertex domain to account for a depression in the scatterer density at the center of the V hyperatom that can be observed in reconstructed Patterson[24–26] and density[29–31] functions. It has been shown recently that the centers of (approximately) icosahedral clusters found in the R-($Al_{0.564}Cu_{0.116}Li_{0.320}$) crystal are empty.[34] Similar clusters are also expected in i-($Al_{0.570}Cu_{0.108}Li_{0.322}$).[38–43] Moreover, positron annihilation experiments[42] and theoretical total energy calculations[48,49] also arrived at the conclusion that the centers of these icosahedral clusters should be empty. Therefore we shall remove the portion of the V hyperatom that corresponds to the atoms at the centers of such icosahedral clusters in physical space. When embedded in the hypercrystal, V atoms that are at the centers of the icosahedra formed by 12 E atoms in physical space map into the portion of the V hyperatom that is the intersection of the inner space projections of the 12 E hyperatoms located halfway along the 12 edges (fivefold axes) emanating from the center of the V hyperatom.[50] The resulting region is exactly a τ^{-3} scaled replica of the entire V hyperatom located at its center. Therefore we shall assume that this region, with the volume $v_{Vi}^{\perp}=\tau^{-9}v_{Vo}^{\perp}=15$ Å^3, is empty. The inclusion of this hole in the model also improves the fit of the diffraction data. Therefore the final volume of the V hyperatom is $v_V^{\perp}=v_{Vo}^{\perp}-v_{Vi}^{\perp}=1136$ Å and the total Al and Cu inner space volume $v_A^{\perp}=v_V^{\perp}+6v_E^{\perp}=5302$ Å^3 is only 3.2% short of its experimental value of $5.48(7)\times10^3$ Å^3. The additional 0.2% comes from the removal of the hole in the V hyperatom.

B. Parametrizing hyperatom compositions

Now that we have completely fixed volumes and shapes of the hyperatoms, we have to determine their chemical compositions $p_{\mu i}$. By considering Eqs. (2.14)–(2.17), we see that only one free parameter remains to be determined by the fit. For example, we can use Eqs. (2.15) and (2.16) to eliminate $p_{\mu,\mathrm{Cu}}$ in favor of $p_{\mu,\mathrm{Al}}$,

$$p_{\mu,\mathrm{Cu}}=1-p_{\mu,\mathrm{Al}},\quad \mu=V,E\ . \tag{3.14}$$

Then we can eliminate $p_{E,\mathrm{Al}}$ in favor of $p_{V,\mathrm{Al}}$, by using Eq. (2.14) either for $i=$Al,

$$n_V p_{V,\mathrm{Al}}+6n_E p_{E,\mathrm{Al}}=n_{\mathrm{Al}}\ , \tag{3.15}$$

or for $i=$Cu,

$$n_V(1-p_{V,\mathrm{Al}})+6n_E(1-p_{E,\mathrm{Al}})=n_{\mathrm{Cu}}\ . \tag{3.16}$$

These two equations would have been equivalent if the volume $v_A^{\perp}$ (or, equivalently, the density n_A) were exact. However, as noted in the previous section, this volume is off by 3.2%. Therefore, if we use Eq. (3.15) to eliminate $p_{E,\mathrm{Al}}$, we shall obtain an exact density for Al and shift the entire 3.2% error to Cu. Conversely, we shall shift the entire error to Al if we use Eq. (3.16). We choose to preserve the Al/Cu stoichiometry and distribute the error in the density accordingly. Thus we eliminate $p_{E,\mathrm{Al}}$ from

$$\frac{n_V p_{V,\mathrm{Al}}+6n_E p_{E,\mathrm{Al}}}{n_V(1-p_{V,\mathrm{Al}})+6n_E(1-p_{E,\mathrm{Al}})}=\frac{n_{\mathrm{Al}}}{n_{\mathrm{Cu}}}=\frac{0.570}{0.108}\ , \tag{3.17}$$

to obtain

$$\begin{aligned}p_{E,\mathrm{Al}}&=\frac{n_{\mathrm{Al}}}{n_{\mathrm{Al}}+n_{\mathrm{Cu}}}\frac{n_V+6n_E}{6n_E}-\frac{n_V}{6n_E}p_{V,\mathrm{Al}}\\&=1.070-0.273p_{V,\mathrm{Al}}\ .\end{aligned} \tag{3.18}$$

C. Fitting and results

Our model of the ideal i-($Al_{0.570}Cu_{0.108}Li_{0.322}$) quasiperiodic structure is completely described by ten parameters: the Al concentration in the V hyperatom, $p_{V,\mathrm{Al}}$, and nine thermal parameters B_{El}^x, B_μ, and $B_\mu^{\perp}$, with $\mu=V$, Et, El, and B. The model structure factor F_t, deduced from Eqs. (A8) and (A9) using Eqs. (2.10) and (2.25), is

$$F_t(\mathbf{Q})=\sum_\mu n_\mu f_\mu(\mathbf{Q})f_\mu^{\perp}(\mathbf{Q}^{\perp})e^{i\bar{\mathbf{Q}}\cdot\bar{\mathbf{r}}_\mu}e^{-\bar{\mathbf{Q}}\cdot\bar{\mathbf{B}}_\mu\cdot\bar{\mathbf{Q}}}\ , \tag{3.19}$$

where the $\mu=V$, B, E_j ($j=1,\ldots,6$), and $\bar{\mathbf{B}}_\mu$ are given in Eqs. (2.5)–(2.9), $f_\mu(\mathbf{Q})$ can be calculated using Eq. (2.11), and $f_\mu^{\perp}(\mathbf{Q}^{\perp})$ is the inner space form factor,

$$f_\mu^{\perp}(\mathbf{Q}^{\perp})=\frac{1}{v_\mu^{\perp}}\int_{v_\mu^{\perp}}e^{i\mathbf{Q}^{\perp}\cdot\mathbf{r}^{\perp}}d^3\mathbf{r}^{\perp}\ . \tag{3.20}$$

This inner space Fourier transform is easy to obtain in a closed analytical form for polyhedral hyperatoms.[51] Clearly, for E hyperatoms, only a Fourier transform of a "standard" E hyperatom needs to be calculated. If g_j transforms a "standard" E hyperatom to the one along

the jth edge, then

$$f^{\perp}_{E_j}(\mathbf{Q}^{\perp})=f^{\perp}_{E}(g_j^{-1}\mathbf{Q}^{\perp}) . \tag{3.21}$$

Since the experimental diffraction intensities $I_e(\mathbf{Q})$ are not usually measured in absolute units, the model structure factors need to be scaled by a factor s before a comparison between the experimental and the model diffraction intensities can be made. We shall determine the scale s and the ten parameters described above using the least squares to fit the experimentally measured density I_e by the model intensity $I_t=|(1/s)F_t|^2$,

$$\chi^2\equiv\min_{s,p,\mathrm{B}}\sum_{\mathbf{Q}}\frac{[I_e(\mathbf{Q})-I_t(\mathbf{Q})]^2}{\sigma^2_{\mathbf{Q}}} , \tag{3.22}$$

where $\sigma_{\mathbf{Q}}$ is the experimentally observed standard deviation for $I_e(\mathbf{Q})$.

Although some larger data sets were available to us, we used the data of Ref. 25 because we had information on both the stoichiometry and mass density only for its sample.[32] The data contained 56 x-ray and 40 neutron symmetry-independent diffraction intensities. While each of these two data sets is relatively small, they complement each other. For example, while the x-ray data set might be insufficient to resolve a contribution from such a weak x-ray scatterer as Li, the neutron set can help isolate Li, since Li, unlike Al and Cu, has a negative neutron-scattering length. We fitted the two data sets independently in order to gain some additional insight about the model from the differences in the obtained values of the parameters. Our fitting results for the x-ray- and neutron-diffraction data sets are summarized in Tables I–III. For the x-ray atomic form factors $f_i(Q)$ (i=Al, Cu, Li) at nonzero Q, we used a quadratic interpolation of the values given in Ref. 45 for a fixed set of Q's. These values included the anomalous dispersion. Of course, the exact values at $Q=0$ are $f_{\mathrm{Al}}(0)=13$, $f_{\mathrm{Cu}}(0)=29$, and $f_{\mathrm{Li}}(0)=3$ electrons. Such interpolation was not needed for the neutron-scattering lengths which

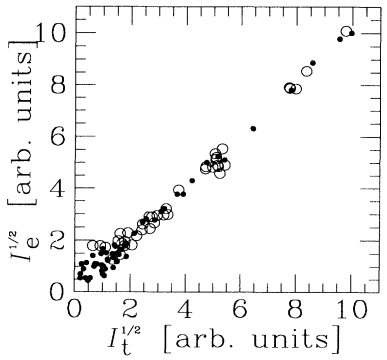

FIG. 5. The scatter graphs of square root of the experimentally measured intensities I_e vs the square root of the model intensities I_t for x-ray- (dots) and neutron- (circles) scattering data.

are constant and, for the given isotope content of the sample, $f_{\mathrm{Al}}=0.3449\times10^{-4}$ Å, $f_{\mathrm{Cu}}=0.7718\times10^{-4}$ Å, and $f_{\mathrm{Li}}=-0.190\times10^{-4}$ Å.[25,32]

In addition to the χ^2 measure of the goodness of the fit, we also calculated and listed in Table III the residual factors which are more commonly used in crystallography,

$$R_F=\frac{\sum_{\mathbf{Q}}|\sqrt{I_e(\mathbf{Q})}-\sqrt{I_t(\mathbf{Q})}|}{\sum_{\mathbf{Q}}\sqrt{I_e(\mathbf{Q})}} , \tag{3.23}$$

$$R_{F^2}=\frac{\sum_{\mathbf{Q}}|I_e(\mathbf{Q})-I_t(\mathbf{Q})|}{\sum_{\mathbf{Q}}I_e(\mathbf{Q})} , \tag{3.24}$$

$$WR=\left[\frac{\sum_{\mathbf{Q}}[I_e(\mathbf{Q})-I_t(\mathbf{Q})]^2/\sigma^2_{\mathbf{Q}}}{\sum_{\mathbf{Q}}I_e(\mathbf{Q})^2/\sigma^2_{\mathbf{Q}}}\right]^{1/2} . \tag{3.25}$$

The quality of the fit we obtained can be also assessed

TABLE VI. Distances and frequencies for icosahedral atomic clusters in physical space centered at a V hyperatom. The first column gives the source of the model while the second column gives frequency of the cluster per atom of the structure. Next, for each of the four shells surrounding the central site, we list the number of atoms in the shell and their hyperatom label, followed by the radius of the shell. For completeness, we also list in the first row data for R-$(Al_{0.564}Cu_{0.116}Li_{0.320})$ with the labeling from Table IV (Ref. 34).

Ref.	n (%)	Orbit	r (Å)
34	1.25	12 (No. 1)	2.516
		8 (No. 2)	4.514
		12 (No. 3)	4.539
		12 (No. 4)	5.046
		48 (No. 5)	6.603
		12 (No. 6)	7.081
This paper/Appendix C/Appendix D	0.2/1.1/1.0	12E	2.528
	(1.6/0.3/0.8)[a]	20B	4.604
		12V	5.056
		60E	6.587

[a]Additional frequency of this shell when the central V atom is present and the other shells are incomplete, losing the full icosahedral symmetry.

visually by constructing the scatter graphs $\sqrt{I_e}$ versus $\sqrt{I_t}$, shown in Fig. 5.

The determined hypercrystal structure model represents a concise record of the real quasicrystal structure, and in principle, one can calculate locations of every atom in physical space by cutting through the hypercrystal. However, it is also useful to address some of the average aspects of the quasicrystal structure relevant to the physical properties. For example, using the formulation given in Appendix A, one can determine the radial distribution function for the shortest interatomic separations found in the model. These occur in the high-symmetry clusters shown in Fig. 6. The frequencies of these clusters can be also calculated as explained in Appendix A, and a comparison with the frequencies of similar clusters in R-$(Al_{0.564}Cu_{0.116}Li_{0.320})$ can be made as shown in Table VI.

IV. DISCUSSION

In this section we shall demonstrate that physical implications of the values obtained for the parameters in our model are reasonable. They are also found to be consistent with the solutions of the phase problem.[29,30] A detailed comparison with other models shows that although a large percentage of atoms has identical positions in all models, there are important differences. For example, while some of the models give better R factors than our model, they all have either larger errors in density or stoichiometry, or unphysically short interatomic distances. Finally, we partially address the question of interpretation of the structure in the physical space by relating it to a simple tiling model.

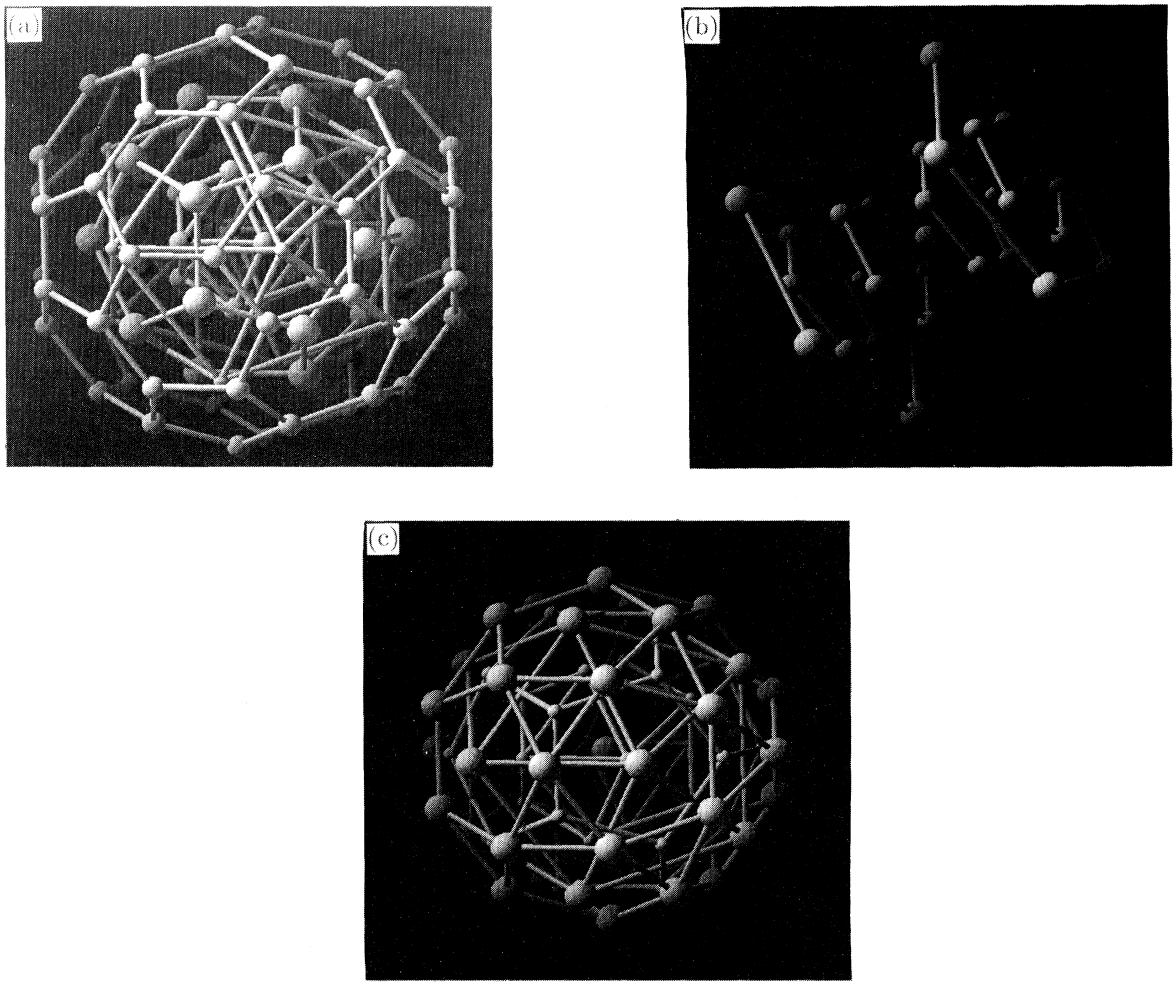

FIG. 6. High-symmetry atomic clusters found for our model in the physical space centered at a (a) vertex, (b) midedge, or (c) a body center of the hypercrystal. All three clusters are shown on the same scale. Atoms originating from V hyperatoms are shown with the smallest spheres, while these from B hyperatoms are shown with the biggest spheres. For clarity, atoms in the same shell are connected.

A. Evaluation of the results

Our fit produced $R_F=0.068$ for the neutron- and $R_F=0.123$ for the x-ray-diffraction data. According to the usual standards of crystal structure determination, these values indicate that the resulting model can be used as a good starting point for a more detailed modeling and refinement. Although both data sets should be simultaneously fitted in the final refinement, by comparing the R factors of the two independent fits, we can conclude from the considerably worse fit of the x-ray data that major corrections to the model should be made in the final refinement for Al. Namely, Li is a very weak x-ray scatterer and could not affect the x-ray fit, while Cu as the dominant scatterer for both x-rays and neutrons would affect both fits similarly. Therefore the only remaining candidate is Al, which makes a relatively larger contribution to x-ray scattering, where Li is negligible, than to neutron scattering, where Li makes a comparable contribution.

This conclusion is consistent with the embedding of R-$(Al_{0.564}Cu_{0.116}Li_{0.320})$ into the hypercrystal that gives pure Al near body centers, which we neglected as explained in Sec. II. Furthermore, as evidenced in Table I, the Al content of the V and E hyperatoms, obtained from x-ray- $[p_{V,Al}=0.64(1),\ p_{E,Al}=0.896(3)]$ and neutron-diffraction fits $[p_{V,Al}=0.77(6), p_{E,Al}=0.86(2)]$, is qualitatively consistent with the embedding. Indeed, the E hyperatom is in both cases richer in Al than the V hyperatom, like the embedding would suggest $[p_{V,Al}=0.54(1), p_{E,Al}=0.886(6)]$. The overall increase in the concentration of Al on the V and, to a lesser extent, on the E hyperatoms can be again ascribed to our neglecting Al near the B hyperatom and, thus, transferring it mostly into the V and, significantly less, into the E hyperatoms.

The values for the physical space thermal fluctuations listed in Table II for x-ray data, B_μ between 0.0117(4) and 0.015(2) Å^2, correspond to the rms atomic displacements between 0.257(1) and 0.355(3) Å and are in the upper range of values commonly observed in crystals. For example, the eigenvalues of the thermal motion tensors in the related R-$(Al_{0.564}Cu_{0.116}Li_{0.320})$ crystal range between 0.007 and 0.013 Å^2.[34] The values of B_μ between 0.0110(8) and 0.020(2) Å^2, listed in Table II for neutron data, are in the similar range as for the x-ray data. Note that like in ordinary crystals, the values of thermal fluctuations obtained with x-ray- and neutron-diffraction experiments are generally different.

The inner space thermal tensors $B_\mu^\perp$ listed in Table II span a much larger range, between 0.00(5) and 0.41(7) Å^2, for x-rays and between 0.0(1) and 3(1) Å^2 for neutrons. The inner space fluctuations $B_\mu^\perp$ can be translated into rms percentages of the atoms which are rearranged in physical space,[29]

$$\frac{\Delta n_\mu}{n_\mu}\sim\frac{1}{2\sqrt{\pi}}\frac{(B_\mu^\perp)^{1/2}}{(v_\mu^\perp)^{1/3}}\ , \tag{4.1}$$

giving an acceptable range of values for x rays (2% for V, 1% for E, and 0% for B) and neutrons (1% for V, 0% for E, and 4% for B). While it could be argued, like for ordinary fluctuations, that there should be generally a difference between the x-ray and neutron values of $B^\perp$, their large uncertainties should also contribute to the observed disparities. These large uncertainties are caused by the very narrow range of $\mathbf{Q}^\perp$'s for which measurable diffraction peaks are observed, causing a limited sensitivity of the fit and a shallow minimum with respect to $B_\mu^\perp$.

For both x-ray and neutron data fits, we find nonzero values of the cross term in the longitudinal components of the E thermal tensors, $B_{El}^x=0.012(3)$ Å^2 and $B_{El}^x=-0.004(3)$ Å^2, respectively. This means that a rearrangement of atoms in physical space associated with the inner space fluctuations of an E hyperatom is generally accompanied by a displacement of the rearranged atom.

B. Comparison with phase problem solutions

Our modeling results can be also compared with our earlier independent solutions of the phase problem.[29,30] Two different methods were used to solve the problem and reconstruct structure factors. The rational approximant method was used for both x-ray- and neutron-diffraction data,[29] while the inner space method was applied only to the neutron data.[30] Both methods yield the unknown phases $\theta(\mathbf{Q})$ of the structure factors and the scale factor s. The first method also provides values of the overall physical and inner space Debye-Waller (DW) parameters B and $B^\perp$, while the values of the cross term B_{El}^x and of B_μ for each hyperatom can be determined with the second method.

For the purpose of a comparison, we construct in Fig. 7 scatter graphs showing structure factors F_t calculated for our model versus the structure factor F_r reconstructed by the two methods for solving the phase problem. For the method of Ref. 29, we used $F_r(\mathbf{Q})=s\sqrt{I(\mathbf{Q})}e^{i\theta(\mathbf{Q})}$, while, for the method of Ref. 30, F_r was calculated using the parametrization given there. The overall slope is approximately unity in all cases, indicating consistency of the calculated scale factors s. Indeed, the values found for the neutron data are $7.2(2)\times10^{-8}$ Å^{-2} in our model, $7.4(1)\times10^{-8}$ Å^{-2} in the rational approximant method,[29] and $7.1(5)\times10^{-8}$ Å^{-2} in the inner space method.[30] Similarly, for x-ray data, the scale found here is $1.69(1)\times10^{-2}e/$Å^3, while it is $1.77(3)\times10^{-2}e/$Å^3 in Ref. 29. It can be also seen from the scatter graphs, Fig. 7, that only two of the smallest x-ray and neutron structure factors are found to have inconsistent phases with the ones determined by the solutions of the phase problem. Specifically, the inconsistencies are found with the rational approximant method for the x-ray $(2221\bar{1}\,\bar{1})$ and (333001) Bragg spots whose measured intensities are only about 0.3% of the strongest intensity. The intensities of the neutron $(2221\bar{1}1)$ and (333002) Bragg spots that have inconsistent phases with the inner space method are, respectively, about 5% and 3% of the strongest measured intensity.

As can be seen from Table II, the values obtained for B_μ and B^x in our model are typically within two standard deviations of the values obtained with the solutions of the

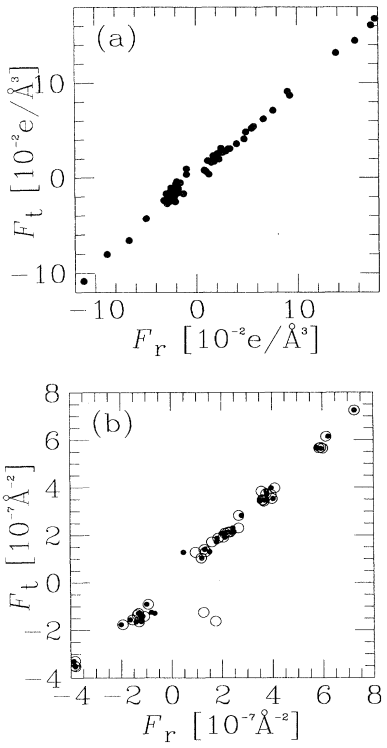

FIG. 7. Scatter graphs of the (a) x-ray and (b) neutron model structure factor F_t vs the structure factors F_r calculated using the rational approximant (dots) (Ref. 29) and the inner space (circles) (Ref. 30) solutions of the phase problem.

phase problem. The agreement between $B^{\perp}$ values, for which there are large uncertainties discussed earlier, is not as good, especially for x rays. Although the two methods for solving the phase problem do not yield chemical compositions of i-$(Al_{0.570}Cu_{0.108}Li_{0.322})$ hyperatoms, the inner space method leads us to the conclusion that the B hyperatom could not be pure Li.[30] This conclusion is also consistent with the one that we drew from the modeling results, namely, that some Al must be present near the B hyperatom. Therefore we find that our structure model of i-$(Al_{0.570}Cu_{0.108}Li_{0.322})$ and its implications are, on the whole, consistent with our earlier solutions of the phase problem of i-$(Al_{0.570}Cu_{0.108}Li_{0.322})$.[29,30]

C. Other models

The results of our modeling can be compared with structural models proposed for i-$(Al_{0.570}Cu_{0.108}Li_{0.322})$ by other researchers. As mentioned in the Introduction, the main difficulty in the comparison is presented by the fact that different models are often fitted to different, sometimes poorly characterized samples. Different samples have different hyperlattice constants, densities, and stoichiometries. Also, different parametrizations are sometimes used for different models. Four different x-ray data sets, for four samples, and a neutron data set, for one of the samples, were used by several groups of researchers to produce nine different structural models. The majority of these models are based on the Ammann tiling decorated directly in physical space[20,21,23] or on its lifting and "decoration" in hyperspace,[22,24] as we did in Appendix C. However, several models are formulated directly in hyperspace unprejudiced by any tiling picture in the physical space. In addition to our model presented in the main text, these are the model of Ref. 25 and the model we constructed in Appendix D.

Tiling models of the icosahedral Al-Cu-Li phase are based on the Ammann tiling and adaptations of the basic tiling motifs originally suggested for the icosahedral $(AlZn)_{49}Mg_{32}$ quasicrystal.[43] Over 20 independent x-ray-powder-diffraction intensities, indexed using hyperlattice constant $\bar{a}=7.132$ Å ("quasilattice" constant $a=\bar{a}/\sqrt{2}=5.043$ Å), were observed in Ref. 20 for a sample with stoichiometry i-$(Al_{0.561}Cu_{0.102}Li_{0.337})$ and an unreported mass density. These data were compared with the Amman tiling model that ignores Li and places an "average" $Al_{0.561}Cu_{0.102}$ atom at all vertices and edge centers of the tiling. The resulting $R_F=0.11$ was calculated in Ref. 23 considering 20 (presumably strongest) diffraction peaks. The model was further refined by optimizing the overall scale and DW parameters of Al and Cu, resulting in $R_F=0.10$. However, neither the resulting scale nor the DW parameters were reported in Ref. 23.

This model was further extended in Ref. 23 by adding two atomic sites that divide the long diagonal of the prolate Ammann rhombohedron in the ratio τ:1:τ. The model was optimized to fit 37 independent x-ray-diffraction intensities indexed using $\bar{a}=7.126$ Å ($a=5.039$ Å) for a sample with unknown stoichiometry and density. Optimization of the overall scale, DW parameters of Al, Cu, and Li, and of chemical compositions on each of the three types of sites (vertex, edge center, and body diagonal) resulted in $R_F=0.07$. For the sake of modeling, stoichiometry was arbitrarily fixed to i-$(Al_{0.6}Cu_{0.1}Li_{0.3})$, resulting in an overall mass density of 2.633 g/cm^3. A more accurate calculation of the structure factors for this model was performed by lifting it into hyperspace and using a different sample with 97 observed diffraction peaks.[24] The same stoichiometry i-$(Al_{0.6}Cu_{0.1}Li_{0.3})$ was *assumed* again, and the density remained unknown ($\bar{a}$ was not listed and is presumed here to be the same as in Ref. 23). One parameter was added to allow for a possible displacement of the atoms on the body diagonal of the prolate rhombohedron away from the "ideal" ratio τ:1:τ, but this did not yield any significant improvement of the R factor when considering the same 37 peaks. While all optimization parameters, except the overall scale, were listed for this model, their uncertainties were not given and we were unable to decipher consistent units for the DW parameters.[23,24] Significantly, it is stated[24] that no satisfactory fit was possible when considering all 97 of the observed independent peaks.

The main difficulty with this model is that it allows for chemical disordering among all three species Al, Cu, and Li, which does not occur in the related crystal of R-$(Al_{0.564}Cu_{0.116}Li_{0.320})$ and seems unlikely in view of the

large differences in the atomic sizes. In order to remedy this deficiency and obtain all optimized parameters and their uncertainties, we adapted this model by restricting the body diagonal sites to pure Li while excluding Li from the vertex and edge center sites. Furthermore, we wanted to compare this model, described more fully in Appendix C, with the model we presented in the text. Therefore we optimized the parameters by fitting the same 56 independent x-ray and 40 independent neutron peaks measured in Ref. 25 (with $\bar{a}=7.15$ Å and $a=5.056$ Å) for the same sample we study here [that is, i-($Al_{0.570}Cu_{0.108}Li_{0.322}$) and $\rho=2.46$ g/cm^3 (Ref. 32)]. The optimization for both x-ray and neutron data results in a rather poor overall fits with $R_F=0.137$ and 0.089, respectively.

The most sophisticated derivative of the simple Ammann tiling model, more closely related to the tiling motifs of Ref. 43, was constructed in Ref. 22, and its parameters were fitted simultaneously to the same x-ray and neutron data we used here, yielding $R_F=0.076$ and 0.085, respectively. The main difference between the model of Ref. 22 and the simple tiling model is that in Ref. 22 some Al/Cu atoms are removed from certain vertices and edges of the Ammann tiling, while some additional Li and Al atoms are added at other special positions. When viewed as a hypercrystal, this model, like the one in Appendix C, has Al/Cu hyperatoms at vertices and half edges and a Li hyperatom at body centers of the hypercubic unit cell. However, it also has an additional 30 Al hyperatoms surrounding the Li hyperatom along the 30 twofold axes. The description of this model in Ref. 22 is quite complete, allowing for its detailed analysis and a comparison with our model.

The most complex of the tiling models of i-($Al_{0.570}Cu_{0.108}Li_{0.322}$) is described in Ref. 21. Unfortunately, there is not yet a simple hypercrystal description of this model that might help elucidate its relationship with the other tiling models. Moreover, in contrast to the other models, all of which have the same primitive space group symmetry $P53m$, this model has a different, face-centered, symmetry. An analysis of this model is further hampered by the absence of a detailed information about the values of its fitting parameters. However, for all its complexity, this model provides a rather poor fit to both x-ray and neutron data ($R_F=0.16$ and 0.13, respectively).

A hypercrystal model of i-($Al_{0.570}Cu_{0.108}Li_{0.322}$) given in Ref. 25 has a spherical Al/Cu hyperatom at the vertices and another ellipsoidal Al/Cu hyperatom at the edge centers of the hypercubic lattice. In addition, there is a Li hyperatom at the body centers. Its shape is determined by starting from a large sphere, adding smaller spheres along the threefold axes, and then removing intersections with some surrounding Al/Cu ellipsoids along the fivefold axes.[52] Although resulting in a relatively low R factors ($R_F=0.08$, for either x-ray or neutron data), this model suffers from the usual difficulty encountered with such simple hyperatom shapes: In order to avoid most unphysically short interatomic distances, the Al, Cu, and Li model densities had to be reduced below their experimentally observed values. This limitation can be alleviated by considering more complex hyperatom shapes, like in the models presented here, in Appendix D, or in Ref. 22.

D. Comparison between models

Our comparison of different models is summarized in Table III where we list the R factors, densities of unphysically short interatomic separations, and differences between the calculated and experimentally determined[32] number densities. When comparing the values of R factors, one should first consider the number of data points that are being fitted. Thus the physical[23] and hyperspace[24] model that results in an R factor of $R_F=0.07$ obtained for the fit of 37 data points is probably better than the rough model[20] that produces $R_F=0.10$ (cf. Ref. 24) for a fit of only 20 data points. However, it is not necessarily better than the model of Ref. 22 that yields $R_F=0.076$ for the fit of 56 data points. In fact, it is possibly worse than most models presented in Table III since it "cannot explain"[24] the enlarged set of 97 data points (resulting, presumably, in $R_F>0.2$).

It is important to emphasize that structural models with violations of stoichiometric or steric constraints are unacceptable, even though they may give better R factors. By comparing different models to our model in Table III, we see that some give a better density of Al, others of Cu, and yet others of Li. Therefore, in addition to evaluating $\Delta n_i \equiv n_i^t/n_i^e - 1$, the departure of the model density n_i^t from the experimental density n_i^e for each chemical component i, we must also evaluate an overall measure $\Delta n=[\sum_i(\Delta n_i)^2]^{1/2}$. Models with the worst R factors (Ref. 21 and Appendix C) have also the largest overall errors Δn, 20.9% and 31.8%, respectively. Although smaller, the overall errors of 10.6%, 9.5%, and 8.6% resulting from the models with the best R factors, Refs. 23, 24, 25, and 22, respectively, are also unacceptable. On the other hand, the error of 4.9% obtained for our model is comparable with the experimental uncertainty of 4.8% and it should be considered acceptable. The error of 6.2% for the model discussed in Appendix D that results in R factors that are slightly better for x rays and slightly worse for neutrons was considered marginally unacceptable here.

By applying our method of systematic examination of steric constraints in the hypercrystal, we discovered unphysically short interatomic separations in two earlier models of the i-($Al_{0.570}Cu_{0.108}Li_{0.322}$) structure that had the most promising R factors. In the model of Ref. 25, we found a 1.931-Å Al/Cu-Li interatomic separation, which is too short. On the average, approximately 0.2% of all atoms in this model have a neighbor at that unacceptably short distance. These separations were apparently missed in a heuristic search through a finite, presumably too small, atomic cluster constructed from the model.[25] We also found an unacceptably short 2.031-Å Al-Al separation in the model of Ref. 22. A fairly large fraction of atoms, around 4%, has an unphysically close neighbor in this model. The presence of these short interatomic separations, together with the large errors in the atomic densities, seriously limit applicability

of the models of Refs. 25 and 22 to *i*-($Al_{0.570}Cu_{0.108}Li_{0.322}$).

Despite failures of the earlier models to satisfy stoichiometric or steric constraints imposed by *i*-($Al_{0.570}Cu_{0.108}Li_{0.322}$), we find that their distribution of chemical species, absolute scales, and Debye-Waller parameters, whenever determined, show the same *trends* seen in our model. This can be also said of the two models described in Appendixes C and D. The hyperatom compositions in different models are summarized in Table I, while the Debye-Waller parameters and the absolute scales (with which they are strongly correlated) are summarized in Table II. For example, except for the neutron fit of the models discussed in Appendixes C and D, all models show a higher concentration of Al at the E than at the V hyperatoms. Similarly, all models have negligible concentration of Li at the V and E hyperatoms.

We could not compare the Debye-Waller parameters B_μ resulting from the fits in several models. The DW parameters of the models in Refs. 20 (determined in Ref. 24) and 21 are not published, while those of the models in Refs. 21, 23, 24 are associated with chemical species, not hyperatoms. Moreover, their units are not indicated in Refs. 23 and 24. With the exception of B_B obtained from x-ray diffraction, all other models generate mutually consistent B_μ's and B^x_{El}. This exception can be easily understood since the B hyperatom is dominated by Li, a weak x-ray scatterer. Consequently, parameters associated with the B hyperatom are at a shallow minimum for x rays and have a large variance.

For a similar reason, a large variation among the values of $B^\perp_\mu$ is found in the models which allow for their determination. In particular, it is difficult to assess the significance of the zero values obtained for several $B^\perp_\mu$ in our models and in models in which they were set to zero based on preliminary fits.[22,25] However, the zero values can be expected in cases where a hyperatom domain $v^\perp_\mu$ in inner space is not touching a hyperatom domain $v^\perp_\nu$ that is of the same chemical type and at a relatively short distance r in physical space. Conversely, directions $\hat{\mathbf{r}}^\perp$ in the inner space which correspond to touching domains of the same chemical type that are at particularly short distances r in physical space should be the softest directions for the inner space ("phason") fluctuations. The separations r in physical space could, indeed, be extremely short, since they do not correspond to a separation between two simultaneously present atoms, but rather to two alternate positions of a single atom.

We can also see from Table II a consistency between the scale factors s determined in different models. As expected, a small variation in the values of the scale s between different models is strongly correlated with a variation in the values of the DW parameters: A decrease of the scale factor is generally associated with an overall increase in the DW parameters.

Although this paper focuses on quasiperiodic structure models, we are compelled to briefly address a recent *periodic,* simple cubic crystal model of *i*-($Al_{0.570}Cu_{0.108}Li_{0.322}$) that claims excellent R factors[11] and appears successful in reproducing other experimental observations.[53] Indeed, this model results in excellent densities, with the values corresponding to our Table III, $\Delta n_{Al}=-0.5\%$, $\Delta n_{Cu}=2.8\%$, and $\Delta n_{Li}=-4.2\%$, which lead to $\Delta n=5.1\%$, only slightly worse than the value we obtained in our model. These densities are calculated using the cubic lattice constant $a_p=95.4$ Å, which is exactly the same as it should be for the $n=6$ rational approximant of any quasiperiodic structure model with the hyperlattice constant $\bar{a}=7.15$ Å (see Appendix B and the next subsection). However, the value of Δn increases to 6.1% if one uses the value of the Amman tile edge length $a_A=5.012$ Å, given elsewhere in the paper, which is inconsistent with the above value of a_p and thus with the original peak indexing[25] (a consistent value would be $a_A=a=5.056$ Å).

In fact, the indexing problem puts a severe limitation on the validity of this model. While the experimental diffraction data of *i*-($Al_{0.570}Cu_{0.108}Li_{0.322}$) are indexed to a precision of 10^{-3} Å^{-1},[25] the above cubic approximant indexing of the data can be only accurate to within $\approx\pi/a_r=16\times10^{-3}$ Å^{-1}. Thus this cubic structure model could be meaningfully evaluated only as a model of the $n=6$ rational approximant of a real quasiperiodic structure, rather than as a model of the quasiperiodic structure itself. Therefore it is necessary to calculate R factors for the approximant rather than for the quasicrystal. However, in addition to the quasicrystal diffraction intensities $I_e(\mathbf{Q})$, phase information $\theta(\mathbf{Q})$ would be also needed in order to reconstruct the "experimental" intensities I_{pe} of the approximant,

$$I_{pe}(\mathbf{Q}')=\left|\sum\sqrt{I_e(\mathbf{Q})}e^{i\theta(\mathbf{Q})}\right|^2, \tag{4.2}$$

as shown by Eq. (B3) in Appendix B.[29] A simplifying assumption that each orbit of diffraction peaks of the approximant arises from a single orbit of the quasicrystal was apparently made in Ref. 11, although it was not explicitly justified. It is an appropriate assumption whenever the quasicrystal intensities for orbits beyond the leading one in the infinite sum in Eq. (4.2) are too weak to be experimentally detected so that $I_{pe}(\mathbf{Q}')\approx I_e(\mathbf{Q})$. However, since each quasicrystal orbit $\{\mathbf{Q}_q\}$ will generally contribute to several orbits $\{\mathbf{Q}'_c\}$ of the approximant ($\{\mathbf{Q}_q\}\rightarrow\cup_c\{\mathbf{Q}'_c\}$), it is first necessary to verify that the intensities $I_{pt}(\mathbf{Q}'_c)$ *and* the phases $\theta(\mathbf{Q}'_c)$ calculated in the model crystal structure are nearly constant for different orbits $\{\mathbf{Q}'_c\}$ that map onto the single orbit $\{\mathbf{Q}_q\}$. Such a verification was not made in Ref. 11.

In order to compensate for the lack of the phase information, Ref. 11 uses an *ad hoc,* uncontrolled approximation procedure to relate the approximant and the quasicrystal diffraction data,

$$I_t(\mathbf{Q}_q)=\frac{1}{m_q}\sum_c m_c I_{pt}(\mathbf{Q}'_c), \tag{4.3}$$

where m_q and m_c are the sizes of the quasicrystal and corresponding crystal orbits, respectively ($m_q=\sum_c m_c$). Therefore the excellent R factors $R_{F^2}=0.061$ ($WR=0.104$), for x rays, and $R_{F^2}=0.066$ ($WR=0.104$), for neutrons, obtained in Ref. 11 after fitting the quasi-

crystal to the model using Eq. (4.3) are indeed "mysterious" as concluded by the model's authors.[54] However, it should be noted that bigger numbers would be obtained by calculating the appropriate R factors for the *approximant* fit,

$$R_{F^2}=\frac{\sum_q\sum_c m_c|I_e(\mathbf{Q}_q)-I_{pt}(\mathbf{Q}'_c)|}{\sum_q\sum_c m_c I_e(\mathbf{Q}_q)}, \tag{4.4}$$

instead of the R factor

$$R_{F^2}=\frac{\sum_q m_q|I_e(\mathbf{Q}_q)-(1/m_q)\sum_c m_c I_t(\mathbf{Q}'_c)|}{\sum_q m_q|I_e(\mathbf{Q}_q)|}, \tag{4.5}$$

which was calculated for the quasicrystal fit.[11] Indeed, after some elementary manipulations, it is easy to see that the only difference between the two expressions is that the sum over c is taken under the magnitude sign in Eq. (4.5), making it strictly smaller than the expression Eq. (4.4).

E. Structure in physical space

Although a hypercrystal structure model of i-($Al_{0.570}Cu_{0.108}Li_{0.322}$) affords the most economical description, it is the quasiperiodic structure of i-($Al_{0.570}Cu_{0.108}Li_{0.322}$) in physical space that is required for most physical applications. While this physical space structure can be easily obtained from the hypercrystal structure, in order to really "understand" it, one would like to have a more intuitive, chemical description based, for example, on packing considerations. Most models that we reviewed here[20–24] and the model presented in Appendix C are essentially packing models.

The most rudimentary packing (tiling) picture for any structure model with a finite number of local environments, like in our model, can be obtained by ascribing (generalized) Voronoi polyhedra to the atoms, with the linkages between the atoms being specified by the facets of the polyhedra. Already a statistics of the obtained polyhedra provides useful physical information about the structure. However, since the purpose of our model is to serve only as a basis for a future refinement which is to produce the definitive structure model, we have not attempted a packing interpretation. Instead, we only investigated several simple structural aspects of the model.

For example, we have determined typical local environments shown in Fig. 6 that are found at some of the highest-symmetry sites in our structure. The frequencies of the V cluster, calculated using the methodology developed in Appendix A, are listed in Table VI. The four icosahedrally symmetric shells around the empty vertex site shown in Fig. 6(a) are essentially identical to the four nearly icosahedral shells found in R-($Al_{0.564}Cu_{0.116}Li_{0.320}$).[34] Except for the small shifts of the atoms, the main difference is that the six pairs of the Al/Cu atoms in the fourth shell near the three mutually perpendicular twofold axes are replaced in R-($Al_{0.564}Cu_{0.116}Li_{0.320}$) by Al. While the frequency of the icosahedral cluster is considerably smaller than in R-($Al_{0.564}Cu_{0.116}Li_{0.320}$), it should be noted that this is compensated by similar clusters that have a V atom at their centers, the identical fully icosahedral second shell, but slightly incomplete other shells. Also, the frequency, of the icosahedral cluster is smaller than it is in R-($Al_{0.564}Cu_{0.116}Li_{0.320}$) because many other clusters occur in i-($Al_{0.570}Cu_{0.108}Li_{0.322}$). For example, the D_{5d} and Y_h shells shown in Figs. 6(b) and 6(c), centered at the atoms associated with the centers of the E and B hyperatoms, have no counterparts in R-($Al_{0.564}Cu_{0.116}Li_{0.320}$). Although some shells in Fig. 6(c) occur with zero frequency as shown, they occur with a finite frequency when slightly incomplete.

It is clear that all models that we reviewed here will give identical locations for a large fraction of atoms. Namely, the fraction of atoms associated with a hyperatom in one model that is located at identical positions with the atoms of the corresponding hyperatom in another model is equal to the fraction of the volume that is common to the two hyperatoms. In particular, we can view our model in terms of its departures from the simple Ammann tiling model (Appendix C). Keeping in mind the coarsest parametrization we used in the modeling of the B hyperatom, we can argue that our model shows a similar relationship to the Ammann tiling model as does the more detailed model of Ref. 22. Namely, the B hyperatoms of both models can be constructed from the Ammann tiling of Appendix C by taking parts mainly from the long diagonals of the rhombic facets of the V and E hyperatoms (see Fig. 8), and then adding them to the rhombic facets of the B hyperatom. Since we ignore Al at the body center, there is no transfer from the equatorial rhombic facets of E hyperatoms to the B hyperatom along twofold axes in our model as there is in the model of Ref. 22.

Finally, a physical interpretation of quasiperiodic structure models can be obtained by constructing their periodic approximations, the so-called rational approximants, as described in Appendix B. Rational approximants are also useful in various numerical calculations of physical properties, such as calculations of electronic states,[48,55] which often require periodic boundary conditions. Because of the large overlap between the hyperatoms of different hypercrystal models of i-($Al_{0.570}Cu_{0.108}Li_{0.322}$), the two lowest-order rational approximants of the models should mostly coincide with the ones obtained in Ref. 22. Except for some displacements of the atoms, the lowest-order rational approximant of the model of Ref. 22 coincides with R-($Al_{0.564}Cu_{0.116}Li_{0.320}$). Similarly, the lowest rational approximant of our model also reproduces R-($Al_{0.564}Cu_{0.116}Li_{0.320}$), except for the absence of pure Al in our model, as we already explained above in the discussion of Fig. 6(a). Significant differences between competing models would start appearing only for higher-order approximants.

V. CONCLUSIONS

We presented a quasiperiodic atomic structure model of i-($Al_{0.570}Cu_{0.108}Li_{0.322}$) that we constructed directly in

hyperspace, unprejudiced by any tiling assumptions in physical space. After evaluating other quasiperiodic crystal models by focusing on stoichiometric and steric constraints, we concluded that the model presented in this paper has atomic densities closest to the experimentally determined ones, and it has no unphysically short interatomic distances. Although our model is qualitatively close to the modified Ammann tiling model of Ref. 22, we discovered that unlike our model, this model and the model of Ref. 25 both contain unphysically short interatomic distances. Moreover, our model has the best R factor for the fit of the neutron-scattering data. Consequently, we conclude that our model is an excellent candidate for the final refinement and determination of the definitive structure model of i-$(Al_{0.570}Cu_{0.108}Li_{0.322})$. The refinement should incorporate positive aspects of our model, as well as these of the model of Ref. 22, which may lead to a convincing tiling justification of our model. Our analysis suggests that a somewhat worse R factor obtained for fitting the x-ray data with our model could be best improved, without affecting significantly the neutron data fit, by shifting some Al to the body center position in the hypercrystal. Following the arguments in Ref. 22, the refinement should focus on removing parts from the equatorial region of the E hyperatoms, converting them to pure Al and adding them to the twofold axes of B hyperatoms. However, in order to avoid unphysically short Al-Al distances encountered in Ref. 22, these new Al parts of B hyperatoms should not be "flat" in our refinement, i.e., $s_{Al} \neq 0$. An indication that we may need to consider nonflat hyperatoms more generally in the refinement is in the values of the physical space DW parameters obtained in all quasiperiodic models reviewed here. They are somewhat larger than what is seen in the related R-$(Al_{0.564}Cu_{0.116}Li_{0.320})$ crystal, possibly mimicking the nonflatness of the hyperatoms. As we explain in Appendix A, the nonflatness and inhomogeneities of hyperatoms are both caused by differing physical space local environments associated with different portions of a hyperatom. Therefore relaxing the assumptions of flatness and homogeneity of our hyperatoms should be *a priori* equally important in the ultimate refinement of the model presented here. In an extreme case, an initially single hyperatom (e.g., the B hyperatom) might have to be broken into multiple hyperatoms of different chemical composition (e.g., Al and Li).

ACKNOWLEDGMENTS

We are grateful to colleagues at the University of California Santa Cruz for hospitality and use of facilities while a part of this work was carried out, to Dr. T. Soma for discussions and assistance, and to M. de Boissieu for helping us clarify some parts of Ref. 25 by providing unpublished information.[52] This research was supported in part by the NSF Grant Nos. DMR8821802 and DMR9215231.

APPENDIX A: FROM QUASICRYSTAL TO HYPERCRYSTAL AND BACK

As it is well known, a three-dimensional quasiperiodic crystal can be viewed as a cut through a higher, D-dimensional ($D>3$) periodic crystal (hypercrystal).[15–19] The quasiperiodicity dictates that the cut is not parallel to any of the crystallographic planes of the hypercrystal. The structure of the hypercrystal can be constructed by embedding the atoms of the quasicrystal into the hypercrystal and imposing the periodicity of the hypercrystal. Clearly, such a representation is the most meaningful if the embedding of the locations of the physical atoms results in an extended, piecewise continuous surface with only a finite (small) number of pieces per unit cell of the hypercrystal. Each continuous piece of the surface, which we call a "hyperatom," represents a concise record of infinitely many distinct atomic positions in the real quasicrystal. If the cut through the hypercrystal is to produce pointlike atoms in three-dimensional physical space, the hyperatoms must be extended objects of codimension 3 transverse to physical space. Therefore a hyperatom must be characterized not only by its position and chemical character, but also by its geometrical "shape."

A μth hyperatom can be specified by its position $\bar{\mathbf{r}}_\mu$ within the unit hypercell and by its geometrical shape,

$$\mathbf{r}=\mathbf{s}_\mu(\mathbf{r}^\perp), \quad \mathbf{r}^\perp \in v_\mu^\perp , \tag{A1}$$

where $\bar{\mathbf{r}}$ is measured relative to $\bar{\mathbf{r}}_\mu$ as the origin. (Hereafter, all quantities with an overbar are distinguished as hyperspace quantities, while quantities with a $\perp$ superscript are associated with the "inner space," the orthogonal complement to physical space.) This requires specifying the vector function $\mathbf{s}_\mu(\mathbf{r}^\perp)$ as well as the shape of the $(D-3)$-dimensional domain $v_\mu^\perp$. The volume of this domain, which we shall also denote by $v_\mu^\perp$, determines the number density n_μ of the corresponding atoms in physical space,

$$n_\mu=\frac{v_\mu^\perp}{\bar{v}} , \tag{A2}$$

where $\bar{v}$ is the volume of the unit hypercell. Obviously, these number densities are constrained by the overall number density n of the quasicrystal by

$$\sum_\mu n_\mu = n . \tag{A3}$$

The average number density n defines characteristic length scales both in physical space, $l \equiv n^{-1/3}$, and in inner space, $l^\perp \equiv (n\bar{v})^{1/(D-3)}$.[29]

Since each point $(\mathbf{s}_\mu(\mathbf{r}^\perp),\mathbf{r}^\perp)$ of a hyperatom corresponds to a different point atom in the real physical structure, different regions within a hyperatom will generally correspond to different local environments in physical space. The larger the environments considered, the finer the division within the hyperatom. Therefore the chemical character of a hyperatom, its atomic form factor, and its thermal Debye-Waller factor may all vary along $\mathbf{s}(\mathbf{r}^\perp)$. We can assume that this variation is continuous, any discontinuities being already used to define boundaries of distinct hyperatoms. Let us denote by $p_{\mu i}(\mathbf{r}^\perp)$ the number fraction of the atomic species i at $\mathbf{r}^\perp$ within the hyperatom μ. In chemically disordered compounds, $p_{\mu i}(\mathbf{r}^\perp)$ is not restricted to 0 or 1 for the atomic

species which are chemically mixed in the compound, but its values can range between these two extrema,

$$0 \le p_{\mu i}(\mathbf{r}^{\perp}) \le 1 , \tag{A4}$$

subject to the constraint

$$\sum_i p_{\mu i}(\mathbf{r}^{\perp}) = 1 . \tag{A5}$$

However, these fractions must also obey the constraint imposed by the quasicrystal's stoichiometry,

$$\sum_{\mu} \frac{1}{\bar{v}} \int_{v_{\mu}^{\perp}} p_{\mu i}(\mathbf{r}^{\perp}) dv^{\perp} = n_i , \tag{A6}$$

where n_i is the number density of species i in the compound. Clearly, by summing Eq. (A6) over i and using Eqs. (A5) and (A2), Eq. (A3) is recovered. Therefore the atomic form factor $f_{\mu}(\mathbf{Q},\mathbf{r}^{\perp})$ of a real atom associated with the point $\mathbf{r}^{\perp}$ of the μth hyperatom is given in terms of the usual atomic form factors $f_i(\mathbf{Q})$ of the constituent species by

$$f_{\mu}(\mathbf{Q},\mathbf{r}^{\perp}) = \sum_i p_{\mu i}(\mathbf{r}^{\perp}) f_i(\mathbf{Q}) . \tag{A7}$$

A real quasiperiodic crystal will generally be imperfect due to annealed (thermal) or quenched disorder. We shall assume that such disordering can be described by Gaussian fluctuations of hyperatoms in the hypercrystal characterized by a generalized thermal motion tensor (ellipsoid) $\bar{\mathsf{B}}_{\mu}$, whose physical (B_{μ}) and inner space ($\mathsf{B}_{\mu}^{\perp}$) diagonal blocks, as well as the off-diagonal block (B_{μ}^{x}), will be nonzero in general. This result was first derived for rigidly fluctuating hyperatoms,[36] but, as we described earlier, since different portions of a hyperatom correspond to real atoms with different local environments in physical space, B_{μ} will be generally a continuous function of $\mathbf{r}^{\perp}$. However, if one is concerned only with equilibrated thermal disorder, then the other components of the thermal tensor should be assumed to be independent of $\mathbf{r}^{\perp}$. Otherwise, a transfer of occupancy would occur between atomic site which are arbitrarily distant in physical space. A particular form and number of independent components of the tensors B_{μ}, $\mathsf{B}_{\mu}^{\perp}$, and B_{μ}^{x} depend on the symmetry of the hyperatom site $\bar{\mathbf{r}}_{\mu}$.

There is a one-to-one correspondence between the reciprocal lattice vectors of the hypercrystal, $\bar{\mathbf{Q}}=(\mathbf{Q},\mathbf{Q}^{\perp})$, and the reciprocal lattice vectors of the quasicrystal, $\mathbf{Q}$. By definition, the hypercrystal structure factor $\bar{F}_{\bar{\mathbf{Q}}}$ is equal, up to an overall phase factor, to the quasicrystal structure factor $F_{\mathbf{Q}}$. On the other hand, since the hypercrystal is periodic, its structure factor is given by a straightforward generalization of the usual formula for periodic crystals. Therefore

$$F(\mathbf{Q}) \equiv \bar{F}(\bar{\mathbf{Q}}) = \sum_{\mu} \bar{f}_{\mu}(\bar{\mathbf{Q}}) e^{i\bar{\mathbf{Q}}\cdot\bar{\mathbf{r}}_{\mu}} , \tag{A8}$$

where the sum is over all *hyperatoms* within the unit hypercell, $\bar{\mathbf{r}}_{\mu}$ is location of the μth hyperatom in the unit cell, and $\bar{f}_{\mu}(\bar{\mathbf{Q}})$ its contribution.

The hyperatom form factor $\bar{f}_{\mu}(\bar{\mathbf{Q}})$ has contributions from the hyperatom shape $\mathbf{s}_{\mu}(\mathbf{r}^{\perp})$, its chemical composition $p_{\mu i}(\mathbf{r}^{\perp})$, and its thermal tensor $\bar{\mathsf{B}}_{\mu}(\mathbf{r}^{\perp})$. Putting all these factors together, we find

$$\bar{f}_{\mu}(\bar{\mathbf{Q}}) = \frac{n_{\mu}}{v_{\mu}^{\perp}} \int_{v_{\mu}^{\perp}} f_{\mu}(\mathbf{Q},\mathbf{r}^{\perp}) \times e^{i[\mathbf{Q}^{\perp}\cdot\mathbf{r}^{\perp}+\mathbf{Q}\cdot\mathbf{s}_{\mu}(\mathbf{r}^{\perp})]} e^{-\bar{\mathbf{Q}}\cdot\bar{\mathsf{B}}_{\mu}(\mathbf{r}^{\perp})\cdot\bar{\mathbf{Q}}} dv^{\perp} , \tag{A9}$$

where $f_{\mu}(\mathbf{Q},\mathbf{r}^{\perp})$ is given in Eq. (A7).

Since we will be imposing steric constraints in the modeling of a hypercrystal, it is important that we also review here the formalism for relating the interatomic separations in a quasicrystal to the structure and hyperatom shapes of the related hypercrystal. Formally, the Patterson function of a quasicrystal can be calculated by making the inverse Fourier transform of the absolute square of the structure factors Eq. (A8). However, it is more relevant to the modeling to determine the pair distribution function of a perfect quasicrystal directly in hyperspace.[47]

Consider two hyperatoms, one at $\bar{\mathbf{r}}_{\mu}$ and another one at $\bar{\mathbf{R}}+\bar{\mathbf{r}}_{\nu}$, where $\bar{\mathbf{R}}$ is a hyperlattice translation. Let us further assume that the inner space domains of these two hyperatoms have a nonzero inner space volume overlap, that is,

$$v_{\mu\nu}^{\perp}(\bar{\mathbf{R}}) \equiv v_{\mu}^{\perp} \cap v_{\nu(\mathbf{R}^{\perp}+\mathbf{r}_{\nu}^{\perp}-\mathbf{r}_{\mu}^{\perp})}^{\perp} \neq \emptyset , \tag{A10}$$

where $v_{\mu(\mathbf{r}^{\perp})}^{\perp}$ denotes domain $v_{\mu}^{\perp}$ translated to $\mathbf{r}^{\perp}$. Then there exists a hyperlattice translation $\bar{\mathbf{R}}'$ and an inner space vector $\mathbf{r}^{\perp} \in v_{\mu\nu}^{\perp}(\bar{\mathbf{R}})$, which depends on $\bar{\mathbf{R}}'$, such that the two hyperatoms translated by $\bar{\mathbf{R}}'$ are both cut by the physical space at $\mathbf{r}_{\mu}^{\perp}+\mathbf{r}^{\perp}$. This generates two atoms in physical space, one at the point $\mathbf{R}'+\mathbf{r}_{\mu}+\mathbf{s}_{\mu}(\mathbf{R}^{\perp})$ and another one at $\mathbf{R}'+\mathbf{R}+\mathbf{r}_{\nu}+\mathbf{s}_{\nu}(\mathbf{r}^{\perp}+\mathbf{r}_{\mu}^{\perp}-\mathbf{R}^{\perp}-\mathbf{r}_{\nu}^{\perp})$. Clearly, the separation between these two atoms,

$$\mathbf{r}_{\mu\nu}(\bar{\mathbf{R}},\mathbf{r}^{\perp}) = \mathbf{R}+\mathbf{r}_{\nu}+\mathbf{s}_{\nu}(\mathbf{r}^{\perp}+\mathbf{r}_{\mu}^{\perp}-\mathbf{R}^{\perp}-\mathbf{r}_{\nu}^{\perp}) - \mathbf{r}_{\mu}-\mathbf{s}_{\mu}(\mathbf{r}^{\perp}) , \tag{A11}$$

depends on the overall translation $\bar{\mathbf{R}}'$ only implicitly, through its dependence on $\mathbf{r}^{\perp}$. In fact, there is an infinite number of hyperlattice translations $\bar{\mathbf{R}}'$ and an associated, essentially continuous variation of $\mathbf{r}^{\perp}$ within $v_{\mu\nu}^{\perp}(\bar{\mathbf{R}})$ that correspond to a continuous distribution of atomic separations $\mathbf{r}_{\mu\nu}(\bar{\mathbf{R}},\mathbf{r}^{\perp})$. The density of all such pairs $n_{\mu\nu}(\bar{\mathbf{R}})$ is simply related to the inner space overlap volume $v_{\mu\nu}^{\perp}(\bar{\mathbf{R}})$ by

$$n_{\mu\nu}(\bar{\mathbf{R}}) = \frac{v_{\mu\nu}^{\perp}(\bar{\mathbf{R}})}{\bar{v}} . \tag{A12}$$

More generally,[47] the quasicrystal pair distribution function $G(\mathbf{r})$ can be evaluated by adding contributions from all μ, ν, and $\bar{\mathbf{R}}$,

$$G(\mathbf{r}) = \sum_{\mu\nu} \sum_{\bar{\mathbf{R}}} \frac{1}{\bar{v}} \int_{v_{\mu\nu}^{\perp}(\bar{\mathbf{R}})} \delta(\mathbf{r}-\mathbf{r}_{\mu\nu}(\bar{\mathbf{R}},\mathbf{r}^{\perp})) dv^{\perp} , \tag{A13}$$

where the sum excludes the $\mu=\nu$, $\bar{\mathbf{R}}=0$ case. In the special case of interest in this paper when hyperatoms are

"flat," that is $\mathbf{s}_\mu(\mathbf{r}^\perp)\equiv 0$, then $\mathbf{r}_{\mu\nu}(\bar{\mathbf{R}},\mathbf{r}^\perp)=\mathbf{R}+\mathbf{r}_\nu-\mathbf{r}_\mu$ is independent of $\mathbf{r}^\perp$ and the pair distribution function reduces to a discrete sum,

$$G(\mathbf{r})=\sum_{\mu\nu}\sum_{\bar{\mathbf{R}}} n_{\mu\nu}(\bar{\mathbf{R}})\delta(\mathbf{r}-\mathbf{r}_{\mu\nu}(\bar{\mathbf{R}}))\ . \tag{A14}$$

APPENDIX B: FROM QUASICRYSTAL TO CRYSTAL AND BACK

A periodic crystal structure with the pair distribution function similar to the one of the quasiperiodic quasicrystal structure can be often obtained in physical space by a "rational" linear distortion of the hypercrystal structure in hyperspace.[29] Such periodic crystal structures, so-called rational approximants, are useful from both theoretical and experimental points of view. On the theoretical side, rational approximants can be used effectively in computer calculations of quasicrystal's physical properties that often require application of periodic boundary conditions. On the experimental side, a rational approximant can be often identified with a real periodic crystal that is closely related to the quasicrystal.

As a hypercrystal is deformed with a shear E^x parallel to inner space, also the structure of the associated quasicrystal in physical space changes.[56] However, since hyperatoms that are flat remain flat under such a shear, the interatomic separations remain the same in the distorted quasicrystal; only their frequencies change. For sufficiently small shears $\mathsf{E}^x \ll l^\perp/l$, only small changes of order $O(\mathsf{E}^x)$ will be made. Since purely inner space distortions are inconsequential to the structure in physical space, a similar change in the quasicrystal structure could be accomplished by a rotation of the hypercrystal. However, hyperatoms would not remain flat after such a rotation and *all* interatomic separations in the distorted quasicrystal would change.

If the shear E^x is rational—that is, it brings a three-dimensional hypercrystal plane (a three-plane) into a parallel orientation with physical space—then, by construction, the resulting structure in the physical space will become periodic with the periodicity of that hypercrystal three-plane. Of course, the periodicity would not be destroyed if the "rational" hypercrystal shear were followed by any linear transformation L in physical space. The resulting transformation L can be represented by

$$\bar{\mathsf{L}}=\begin{bmatrix}\mathsf{L} & 0\\ \mathsf{E}^x & 1\end{bmatrix}, \tag{B1}$$

in the coordinate system in which the hyperspace coordinates are given by $\bar{\mathbf{r}}\equiv(\mathbf{r}\mathbf{r}^\perp)$. As arbitrarily small (rational) shears are taken, $\mathsf{E}^x\to 0$ and $\mathsf{L}\to 1$, the original hypercrystal and quasicrystal are recovered.

The reciprocal hyperlattice transforms under this distortion as

$$\bar{\mathbf{Q}}\to\bar{\mathbf{Q}}'\equiv\tilde{\bar{\mathsf{L}}}^{-1}\bar{\mathbf{Q}}\ , \tag{B2}$$

and reciprocal hyperlattice $(D-3)$-planes become parallel to the inner space. Consequently, the one-to-one correspondence between the reciprocal hyperlattice $\{\bar{\mathbf{Q}}'\}$ and the reciprocal lattice $\{\mathbf{Q}'\}$ breaks down: There are infinitely many different $\bar{\mathbf{Q}}'$ with the same projection $\mathbf{Q}'$, each having a different $\mathbf{Q}'^\perp$. Therefore the structure factor of the resulting periodic crystal,

$$F_p(\mathbf{Q}')=\frac{1}{\det\mathsf{L}}\sum F(\mathbf{Q})e^{i\mathbf{Q}^\perp\cdot\mathbf{r}_0^\perp}\ , \tag{B3}$$

involves an infinite sum that extends over all quasicrystal's $(\mathbf{Q},\mathbf{Q}^\perp)$ that satisfy $\tilde{\mathsf{L}}\cdot\mathbf{Q}'=\mathbf{Q}-\tilde{\mathsf{E}}^x\cdot\mathbf{Q}^\perp$. Here we also introduced $\mathbf{r}_0^\perp$, an inner space translation of the hypercrystal. Such a translation is inconsequential for the quasicrystal, but for rational approximants, different $\mathbf{r}_0^\perp$ will generally result in a different structure.

While an atom with the same chemical character as the μth hyperatom is located at a particular $\mathbf{R}+\mathbf{r}_\mu$ in the quasicrystal if and only if $\mathbf{r}_0^\perp-\mathbf{R}^\perp-\mathbf{r}_\mu^\perp\in v_\mu^\perp$, it is located at that point in the distorted quasicrystal if and only if $\mathbf{r}_0^\perp-\mathbf{R}^\perp-\mathbf{r}_\mu^\perp-\mathsf{E}^x\cdot(\mathbf{R}+\mathbf{r}_\mu)\in v_\mu^\perp$. However, just as atomic clusters within a unit cell of a linearly distorted ordinary crystal would adjust to the distortion according to their local environments, small distortions of the hyperatoms $v_\mu^\perp\to v_{\mu\mathsf{L}}^\perp$ may have to accompany the linear distortion $\bar{\mathsf{L}}$ if the resulting rational approximant is to be considered a viable structure for a real periodic crystal. Namely, although the rational approximant has a pair distribution function similar to that of the quasicrystal, if the hyperatoms are not distorted, unphysically short interatomic distances or large voids will generally occur associated with the boundaries of the hyperatom domains $v_\mu^\perp$. The fraction of atoms of type μ that will contribute to either close pairs or voids is on the order of $|\mathsf{E}^x|l_\mu(v_\mu^\perp)^{-1/(D-3)}$, where l_μ is a distance given by Eq. (2.26) characteristic of the nearest forbidden shells defined in Eq. (2.27).[57] Thus the atomic positions in the rational approximant will be given by

$$\{\mathbf{R}+\mathbf{r}_\mu|\mathbf{r}_0^\perp-\mathbf{R}^\perp-\mathbf{r}_\mu^\perp-\mathsf{E}^x\cdot(\mathbf{R}+\mathbf{r}_\mu)\in v_{\mu\mathsf{L}}^\perp\}\ , \tag{B4}$$

where all hyperlattice vectors $\bar{\mathbf{R}}$ and all hyperatom locations $\bar{\mathbf{r}}_\mu$ need to be considered.

Although it may be sometimes possible to remove some of the short bonds or voids by a careful choice of $\mathbf{r}_0^\perp$, distortions of hyperatom shapes will be generally required. However, without invoking a detailed physical calculation of the total energy, it is not obvious whether, or how, the individual hyperatoms must be distorted as the hyperlattice is being distorted. A possible exception may be the case when the hyperatom domain shapes $v_\mu^\perp$ can be directly related to the elements of the unit cell of the hypercrystal. One of the simplest examples is the Ammann tiling whose vertices result from the domain which is the inner space projection of the unit cell of the hypercubic lattice, $v^\perp=\mathsf{P}^\perp\bar{v}$. Then $v_{\mathsf{L}}^\perp$ is simply the projection of the unit cell of the distorted hypercrystal, $v_{\mathsf{L}}^\perp=\mathsf{P}^\perp\bar{\mathsf{L}}\bar{v}$. In general, however, this lack of knowledge about $v_{\mathsf{L}}^\perp$ must be compensated by a judicial elimination or insertion of atoms where unphysical arrangements are discovered in the approximant obtained by the simple assumption $v_{\mathsf{L}}^\perp=v^\perp$.

So far, we discussed how to construct a periodic crystal starting from a quasicrystal. However, by inverting the

linear transformation $\bar{L}$, a given periodic crystal structure can be lifted into the hypercrystal unit cell to give a discrete set of pointlike atoms. An atom of the periodic crystal located at $\mathbf{r}_k$ in physical space is lifted into a pointlike atom at $\bar{\mathbf{r}}_k$ in hyperspace by

$$\bar{\mathbf{r}}_k=\bar{L}^{-1}\begin{bmatrix}\mathbf{r}_k\\0\end{bmatrix}=\begin{bmatrix}L^{-1}\cdot\mathbf{r}_k\\-\tilde{E}^{x}L^{-1}\cdot\mathbf{r}_k\end{bmatrix}. \tag{B5}$$

Since these pointlike atoms should be located within the $(D-3)$-dimensional hyperatoms, their location and chemical composition may provide useful information about locations, shapes, and compositions of the hyperatoms.

Specifically, we shall consider R-($Al_{0.564}Cu_{0.116}Li_{0.320}$) as a rational approximant of i-($Al_{0.570}Cu_{0.108}Li_{0.322}$).[29] Using the coordinate system given in Ref. 35, the orientation of physical space relative to the hypercubic lattice can be described by the rotation matrix M,

$$\bar{M}=\frac{1}{\sqrt{2}}\begin{bmatrix}\mathbf{e}_1&\mathbf{e}_2&\mathbf{e}_3&\mathbf{e}_4&\mathbf{e}_5&\mathbf{e}_6\\\mathbf{e}_1^{\perp}&\mathbf{e}_2^{\perp}&\mathbf{e}_3^{\perp}&\mathbf{e}_4^{\perp}&\mathbf{e}_5^{\perp}&\mathbf{e}_6^{\perp}\end{bmatrix}$$

$$=\frac{1}{\sqrt{2(\tau^2+1)}}\begin{bmatrix}\tau&\tau&1&0&0&1\\0&0&\tau&1&-1&-\tau\\1&-1&0&\tau&\tau&0\\1&1&-\tau&0&0&-\tau\\0&0&1&-\tau&\tau&-1\\-\tau&\tau&0&1&1&0\end{bmatrix}, \tag{B6}$$

which transforms components of a vector in the Cartesian coordinate system aligned with the hyperlattice to its components in the physical–inner-space coordinate system. By substituting τ with its continued fraction (rational) approximants $\tau_n\equiv F_n/F_{n-1}$, where F_n is a Fibonacci number ($F_{n+2}=F_{n+1}+F_n$, $F_1=F_0=1$), one obtains a sequence of rotations $\bar{M}_n$ that describe hypercrystal orientations with a three-plane parallel to physical space. This corresponds to the rational shears

$$E_n^{x}=[(\bar{M}_n\bar{M}^{-1})^{\perp}]^{-1}(\bar{M}_n\bar{M}^{-1})^{x}=\frac{\tau-\tau_n}{\tau_n\tau+1}I=\frac{(-1)^{n+1}}{\tau^{2n+1}}I, \tag{B7}$$

which, combined with an isotropic physical-space distortion $L=LI$, result in periodic cubic crystals with the lattice constant $a_p=\bar{a}[\tau^{n+1}/\sqrt{2}(\tau+2)]L$. For $n=1$ (mod 3), they are bcc crystals; otherwise, they are sc crystals. By comparing their reciprocal lattices, it follows that the $n=1$ rational approximant of i-($Al_{0.570}Cu_{0.108}Li_{0.322}$), with a small isotropic compression $L=0.999$ in physical space, can be associated with R-($Al_{0.564}Cu_{0.116}Li_{0.320}$).

All pointlike atoms embedded in the unit cell of the hyperlattice can be constructed by first applying Eq. (B5) to a representative atom of each of the seven orbits of atoms in the unit cell of R-($Al_{0.564}Cu_{0.116}Li_{0.320}$). Then additional embedded atoms can be obtained by applying the assumed $P35m$ hypercrystal symmetry in hyperspace. All seven orbits of the R-($Al_{0.564}Cu_{0.116}Li_{0.320}$) atoms can be grouped into three sets in the hypercrystal, associated with the vertex, the six edge centers, and the body center of the hypercubic unit cell. This grouping, shown in Table IV, is accomplished with the separation

$$\bar{\mathbf{r}}_k=\bar{\mathbf{r}}_{\mu(k)}+\Delta\bar{\mathbf{r}}_k, \tag{B8}$$

where, $k=1,\ldots,7$ labels the seven orbits while $\mu(k)=V$, E_j, or B. Obviously, such separation is not unique, and our choice of $\Delta\bar{\mathbf{r}}_k$ represents a compromise so that $|\Delta\mathbf{r}_k|$ is as small as possible while $|\Delta\mathbf{r}_k^{\perp}|\le\frac{1}{2}l^{\perp}\approx 10$ Å.

APPENDIX C: THE AMMANN TILING MODEL

In this appendix, we shall briefly discuss a simple Ammann tiling model of i-($Al_{0.570}Cu_{0.108}Li_{0.322}$) quasicrystal structure and its optimization. Although several variants of the Ammann tiling model have been discussed and utilized for i-($Al_{0.570}Cu_{0.108}Li_{0.322}$),[20–24] they were not fitted to the same data as here or the results of the fitting were not given in sufficient detail. Furthermore, the simple Ammann tiling model discussed here offers a relevant reference point for the model we presented in the main text.

Generally, a tiling model can be described by a prescribed geometric network in physical space and its decoration with atoms. In our case, the network is the Ammann tiling and the atoms will decorate its two rhombohedral building blocks in a similar way that they would decorate the unit cell of a periodic crystal. Although a tiling model of a quasicrystal structure is a very special kind of a model, one that need not describe a real quasicrystal such as i-($Al_{0.570}Cu_{0.108}Li_{0.322}$) in all of its details, we think that studying tiling models may be very helpful. An advantage of the tiling approach is that the global picture of the atomic structure in physical space is built locally and, thus, simplified. Moreover, while a hypercrystal description of the network alone may suffice for a quasiperiodic tiling model, the full hypercrystal description of the tiling as a whole may shed a light on other hypercrystal structure models and their connection to geometrical and topological relationships between the atoms in physical space.

The simplest Ammann tiling model can be constructed by decorating the two Ammann rhombohedra, the prolate and the oblate one. Using our solution of the phase problem for i-($Al_{0.570}Cu_{0.108}Li_{0.322}$),[29,30] we have reconstructed its scatterer density (both for x rays and neutrons).[31] When we superimpose an Ammann tiling over this density and average the density over all prolate or oblate rhombohedra, we find particularly simple distributions using the tile edge length $a=\bar{a}/\sqrt{2}=5.056$ Å. It indicates that the Al/Cu atoms are most likely to occupy vertices and edge centers of the tiling, while the Li atoms are to be found at two sites dividing the long body diagonal of the prolate rhombohedron in the ration $\tau:1:\tau$. These locations of Al/Cu and Li atoms were also suggested earlier by other authors.[20,23] They were found to arise from V, E, and B hyperatoms whose shapes are a rhombic triacontahedron, a rhombic icosahedron, and rhombic hexecontahedron (a stellated polyhedron), respectively.[22,24,44] Their rhombic facets are the same as these of the Ammann rhombohedra in physical space, with an

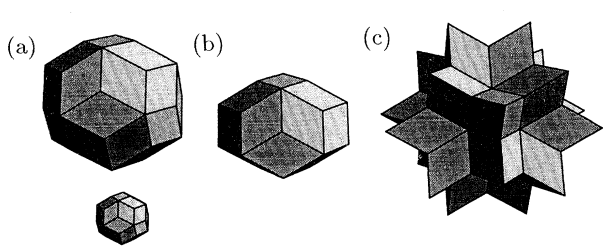

FIG. 8. (a) V, (b) E, and (c) B hyperatoms for the Ammann tiling model of i-($Al_{0.570}Cu_{0.108}Li_{0.322}$) discussed in Appendix C. The small volume in (a) shows the shape of the hole located at the center of the V hyperatom.

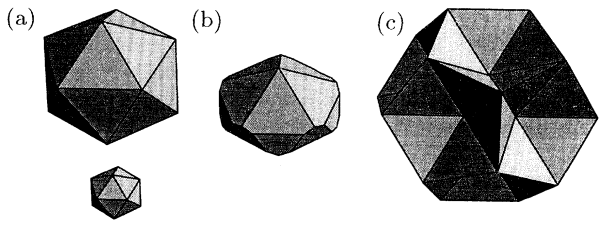

FIG. 9. (a) V, (b) E, and (c) B hyperatoms for the model of i-($Al_{0.570}Cu_{0.108}Li_{0.322}$) discussed in Appendix D. The small volume in (a) shows the shape of the hole located at the center of the V hyperatom.

edge length $a^{\perp}=a=5.056$ Å.

Taking these hyperatom shapes, shown in Fig. 8, and making the same assumptions as in the model presented in the main text, we obtain the results listed in Tables I–III and discussed in Sec. IV. The hyperatoms satisfy the nonoverlap constraints of Figs. 2 and 3, simply because the steric constraints are satisfied by the tiling construction in physical space. However, as shown below, this simple model cannot be consistent with the density observed in the sample, independently of the chemical composition assumed for individual hyperatoms.

Since the volumes of prolate and oblate rhombohedra in inner space (the same as in physical space) are $v_p^{\perp}=2\tau^2\eta^3a^3=98.34$ Å^3 and $v_o^{\perp}=v_p^{\perp}/\tau$, respectively, we can calculate volumes of the rhombic triacontahedron ($v_{Vo}^{\perp}=v_{\text{tria}}^{\perp}=10v_p^{\perp}+10v_o^{\perp}=1591$ Å^3), rhombic icosahedron ($v_E^{\perp}=v_{\text{icos}}^{\perp}=5v_p^{\perp}+5v_o^{\perp}=795.5$ Å^3), and rhombic hexiacontahedron ($v_B^{\perp}=v_{\text{hexia}}^{\perp}=20v_p^{\perp}=1967$ Å^3). Similarly to the arguments given for our model in the main text, we must remove from the center of the V hyperatom its τ^{-2} scaled replica, $v_{Vi}^{\perp}=\tau^{-6}v_{Vo}^{\perp}=88$ Å^3. Thus $v_A^{\perp}\equiv v_V^{\perp}+6v_E^{\perp}=6187$ Å^3, and the total volume $v_T^{\perp}=v_A^{\perp}+v_B^{\perp}=8154$ Å^3. This $v_T^{\perp}$ is only 0.8% larger than the experimental value of $v_{\text{Al}}^{\perp}+v_{\text{Cu}}^{\perp}+v_{\text{Li}}^{\perp}=8.08(9)\times10^3$ Å^3. On the other hand, $v_B^{\perp}$ is 24.5% smaller than the experimental value for Li, $v_{\text{Li}}^{\perp}=2.60(5)\times10^3$ Å^3. As described in the main text, this is a serious problem since all Li and even some Al are expected at the body center. Correspondingly, the $v_A^{\perp}$ volume is 13.0% larger than the experimental value of $v_{\text{Al}}^{\perp}+v_{\text{Cu}}^{\perp}=5.48(7)\times10^3$ Å^3. This discrepancy is exacerbated if some of Al is assumed to reside at the B hyperatom. Therefore any improvement of this simple tiling model should involve removing some volume from the V and E hyperatoms and adding it back to the B hyperatom. Part of it must be converted to Li and another part may be converted to pure Al. Our model and the model of Ref. 22 can both be viewed in this way and are compared in Sec. IV.

APPENDIX D: THE SECOND MODEL

In this appendix we discuss a model with hyperatom shapes shown in Fig. 9. In contrast to the Ammann tiling model where each hyperatom facet is perpendicular to an icosahedral twofold axis, here each facet is perpendicular to a threefold axis. This model results from our parametrization of the B hyperatom shape and the steric constraints of Figs. 2 and 3 described in the main text. By using the same fitting parameters as in the model described in the text, we obtain the results listed in Tables I–III and discussed in Sec. IV. The model produces rather good x-ray and neutron R factors, but, as shown below, is slightly inconsistent with the experimentally measured atomic number densities.

In the same way as we did in the main text, we model the body center hyperatom first. In Eqs. (3.4)–(3.6), we take the longest allowed radii along the twofold and threefold axes, forcing the minimal radius along the fivefold axis; thus, we obtain

$$r_{B5}^{\perp}=a=5.056 \text{ Å} , \tag{D1}$$

$$r_{B3}^{\perp}=\sqrt{3}\eta\tau^2a=12.053 \text{ Å} , \tag{D2}$$

$$r_{B2}^{\perp}=\eta\tau^3a=11.259 \text{ Å} . \tag{D3}$$

By construction, the volume of this hyperatom, $v_B^{\perp}=2574$ Å^3, is the same as for our model described in the main text and, thus, it agrees with the experimental Li volume.

The E and V hyperatoms are bounded by the first two B hyperatom shells, as described in the text, and the resulting hyperatom shapes are shown in Figs. 9(a) and 9(b). The E hyperatom has D_{5d} symmetry and its volume is $v_E^{\perp}=657$ Å^3. Its facets surrounding the two fivefold vertices are truncated equilateral triangles whose two edges that meet at the fivefold vertex are of length $\eta(3\tau-2)a=7.586$ Å, the two short ones are $\sqrt{2}\eta(2-\tau)a=1.436$ Å, and the remaining one is $2\eta a=5.316$ Å. The equatorial facets are also truncated equilateral triangles whose edges crossing the equatorial plane are of length $\eta(\tau-1)a=1.643$ Å, while the other edges are shared with the facets already described.

The V hyperatom is a regular icosahedron of edge $2\eta\tau a=8.602$ Å, also described by the three radial distances

$$r_{V5}^{\perp}=\tau a=8.181 \text{ Å} , \tag{D4}$$

$$r_{V3}^{\perp}=\frac{\eta\tau^3}{\sqrt{3}}a=6.501 \text{ Å} , \tag{D5}$$

$$r_{V2}^{\perp}=\eta\tau^2a=6.959 \text{ Å} . \tag{D6}$$

Its volume is $v_{Vo}^{\perp}=1388$ Å. If we again want to remove from the physical space all V atoms which have the per-

fect 12-fold icosahedral coordination, as described for our model in the main text, we must remove from the center of the V hyperatom its τ^{-2} scaled replica, $v_{Vi}^{\perp}=\tau^{-6}v_{Vo}^{\perp}=77$ Å^3. Then the final volume of the V hyperatom is $v_V^{\perp}=v_{Vo}^{\perp}-v_{Vi}^{\perp}=1311$ Å^3 and the total Al and Cu inner space volume $v_A^{\perp}=v_V^{\perp}+6v_E^{\perp}=5254$ Å^3 is only 4.1% short of the experimental value of $5.48(7)\times10^3$ Å^3. For a comparison, volume of the hole in the V hyperatom is only 1.4% of the experimental value for the Al/Cu volume.

*Present address: Research and Data System Corporation, 7855 Walker Dr., Suite 460, Greenbelt, MD 20770.

[1]D. Schechtman, I. Blech, D. Gratias, and J. W. Cahn, Phys. Rev. Lett. **53**, 1951 (1984).

[2]For a review, see C. L. Henley, J. Non-Cryst. Solids **153**, 172 (1993).

[3]For a review, see C. Janot, *Quasicrystals* (Clarendon Press, Oxford, 1992).

[4]J. C. Jiang, K. K. Fung, and K. H. Kuo, Phys. Rev. Lett. **68**, 616 (1992); **67**, 1302 (1991).

[5]F. Denoyer *et al.*, J. Phys. (Paris) **51**, 651 (1990); C. Beeli, F. Gahler, H.-U. Nissen, and P. Stadelmann, *ibid.* **51**, 661 (1990).

[6]M. Duneau and C. Oguey, J. Phys. (Paris) **50**, 135 (1989).

[7]M. Cornier-Quiquandon, D. Gratias, and A. Katz, in *Methods of Structural Analysis of Modulated Structures and Quasicrystals,* edited by J. M. Perez-Mato, F. J. Zuñiga, and G. Madariaga (World Scientific, Singapore, 1991), p. 313.

[8]C. L. Henley, Phys. Rev. B **43**, 993 (1991).

[9]For a review, see *Extended Icosahedral Structures,* edited by M. V. Jarić and D. Gratias (Academic Press, Cambridge, MA, 1989).

[10]L. Pauling, in *Extended Icosahedral Structures* (Ref. 9), p. 137.

[11]M. Mihalkovič and P. Mrafko, Philos. Mag. Lett. **69**, 85 (1994).

[12]J. L. Robertson and S. C. Moss, Phys. Rev. Lett. **66**, 353 (1991); Z. Phys. B **83**, 391 (1991).

[13]S. E. Burkov, J. Phys. (France) **2**, 695 (1992).

[14]M. Oxborow and C. L. Henley, Phys. Rev. B **48**, 6966 (1993).

[15]D. Levine and P. J. Steinhardt, Phys. Rev. Lett. **53**, 2477 (1984).

[16]P. A. Kalugin, A. Yu. Kitayev, and L. S. Levitov, Pis'ma Zh. Eksp. Teor. Fiz. **41**, 119 (1985) [JETP Lett. **41**, 145 (1985)].

[17]P. Bak, Phys. Rev. Lett. **54**, 1517 (1985).

[18]M. Duneau and A. Katz, Phys. Rev. Lett. **54**, 2688 (1985).

[19]V. Elser, Phys. Rev. B **32**, 4892 (1985).

[20]Y. Shen *et al.*, Phys. Rev. Lett. **58**, 1440 (1987).

[21]P. Guyot, M. Audier, and M. de Boissieu, in *Quasicrystals and Incommensurate Structures in Condensed Matter,* edited by M. J. Yacamàn *et al.* (World Scientific, Singapore, 1990), p. 251; M. de Boissieu *et al.*, in *Quasicrystals,* edited by M. V. Jarić and S. Lundqvist (World Scientific, Singapore, 1990), p. 109.

[22]A. Yamamoto, in *Quasicrystals,* edited by T. Fujiwara and T. Ogawa (Springer, Berlin, 1990), p. 57; Phys. Rev. B **45**, 5217 (1992).

[23]H. B. Elswijk *et al.*, Phys. Rev. B **38**, 1681 (1988).

[24]S. van Smaalen, J. L. de Boer, and Y. Shen, Phys. Rev. B **43**, 929 (1991).

[25]M. de Boissieu *et al.*, J. Phys. Condens. Matter **3**, 1 (1991).

[26]S.-Y. Qui and M. V. Jarić, in *Quasicrystals,* edited by M. V. Jarić and S. Lundqvist (World Scientific, Singapore, 1989), p. 19.

[27]M. de Boissieu, C. Janot, J.-M. Dubois, M. Audier, and B. Dubost, J. Phys. (Paris) **50**, 1689 (1989).

[28]S. van Smaalen, Phys. Rev. B **39**, 5850 (1989).

[29]M. V. Jarić and S.-Y. Qiu, Acta Crystallogr. A **49**, 576 (1993).

[30]M. V. Jarić and S.-Y. Qiu, Phys. Rev. B **49**, 6614 (1994).

[31]S.-Y. Qiu, Ph.D. thesis, Texas A&M University, College Station, 1992; C. R. Rowell, Senior thesis, University of California, Santa Cruz, 1994; S.-Y. Qiu, C. R. Rowell, and M. V. Jarić (unpublished).

[32]B. Dubost, C. Colinet, and I. Ansara, in *Quasicrystalline Materials,* edited by C. Janot and J. M. Dubois (World Scientific, Singapore, 1988), p. 39.

[33]D. Mermin, J. Mod. Phys. **64**, 3 (1992).

[34]M. Audier *et al.*, Physica B **153**, 136 (1988); M. Audier, P. Sainfort, and B. Dubost, Philos. Mag. B **54**, L105 (1986).

[35]M. V. Jarić, J. Phys. (Paris) Colloq. **47**, C3-82 (1986); in *Group Theoretical Methods in Physics,* edited by R. Gilmore (World Scientific, Singapore, 1987), p. 288.

[36]M. V. Jarić and D. R. Nelson, Phys. Rev. B **37**, 4458 (1988).

[37]Some of this variation is caused by the experimentally introduced truncations in the reciprocal space, as discussed in Ref. 27.

[38]Y. Ma, E. A. Stern, and F. W. Gayle, Phys. Rev. Lett. **58**, 1956 (1987); E. A. Stern and Y. Ma, Mater. Sci. Forum **22-24**, 423 (1987).

[39]P. Sainfort and P. Guyot, Scr. Metall. **21**, 1517 (1987).

[40]W. Dmowski *et al.*, Philos. Mag. Lett. **56**, 63 (1987).

[41]C. Lee *et al.*, Phys. Rev. B **37**, 9053 (1988); M. Qing'an *et al.*, Chin. Phys. Lett. **6**, 28 (1989).

[42]T. Ohata *et al.*, Phys. Rev. B **42**, 6730 (1990); I. Kanazawa *et al.*, Mater. Sci. Forum **105-110**, 1093 (1992).

[43]C. Henley and V. Elser, Philos. Mag. B **58**, L59 (1986).

[44]K. N. Ishihar and P. H. Shingu, J. Phys. Soc. Jpn. **55**, 1795 (1986).

[45]*International Tables for Crystallography,* edited by A. J. C. Wilson (Kluwer Academic, Boston, 1992), Vol. C.

[46]Although not unique, this particular truncation of the rhombic triacontahedra appeared in several studies concerned with the packing of spheres [C. L. Henley, Phys. Rev. B **34**, 797 (1986)] or atomic clusters (Ref. 22) on 12-fold vertices of the Ammann tiling.

[47]M. V. Jarić and S. Narasimhan, Phase Transit. **16/17**, 351 (1989).

[48]T. Fujiwara and T. Yokokawa, in *Quasicrystals,* edited by T. Fujiwara and T. Ogawa (Springer-Verlag, Berlin, 1990), p. 196.

[49]R. B. Phillips and A. E. Carlsson, Phys. Rev. B **37**, 10 880 (1988).

[50]Additional restrictions, which would generally reduce the size of this region, can be imposed by extending the requirement of icosahedral symmetry to further neighbors. For example, the second icosahedral shell consists of 12 V atoms, giving rise to the corresponding inner space intersection of 12 V hyperatoms. However, icosahedral shells up to the fourth shell, shown in Fig. 6 and Table VI, do not change the overlap region and, thus, the cluster frequency in our model.

[51]Fourier transform of a polytope in any dimension can be found iteratively by reducing it to the sum of Fourier transforms of its facets, which are polytopes in one less dimension [J. Komrska, Optik **80**, 171 (1987)]. Alternatively, it can be calculated by dividing the polytope into simplexes and then summing over the Fourier transforms of each simplex.

[52]M. de Boissieu (unpublished).

[53]M. Windisch *et al.*, Phys. Rev. B **49**, 8701 (1994).

[54]See Ref. 52 in Ref. 53.

[55]See, for example, T. Fujiwara, G. Trambly de Laissardiere, and S. Yamamoto, Mater. Sci. Forum **150-151**, 387 (1994).

[56]We consider here only active transformations; that is, we transform physical quantities, but leave the space fixed.

[57]This distance l_μ is related to the minimum distance for the separation between alternate positions that a quasicrystal atom takes under a "phason" flip (Refs. 16, 17).

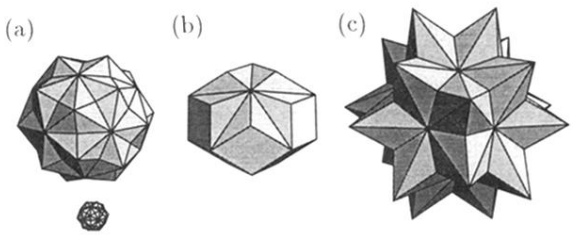

FIG. 1. Shapes of the (a) V, (b) E, and (c) B hyperatoms in our model of i-$(Al_{0.570}Cu_{0.108}Li_{0.322})$ structure. The small volume in (a) shows the shape of the hole located at the center of the V hyperatom.

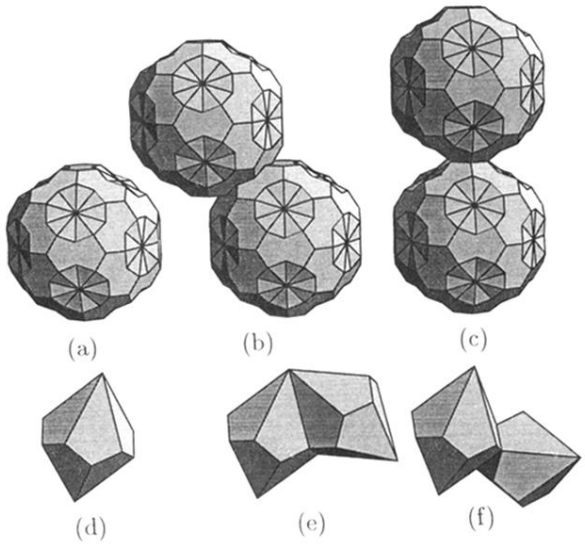

FIG. 2. Outer bounds for the (a) V or B and (d) E hyperatoms, resulting from their respective first [(b), (e)] and second [(c), (f)] second nonoverlap shells.

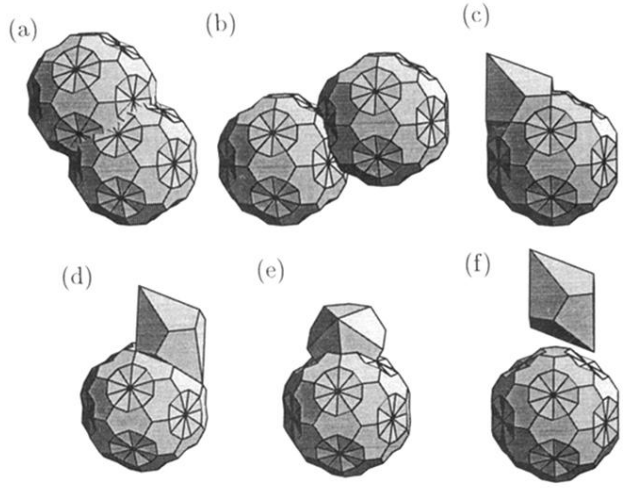

FIG. 3. Relative positions and orientations of the outer bounds in the first [(a), (c), (e)], and second [(b), (d), (f)], *B-V* [(a), (b)], *B-E* [(c), (d)], and *V-E* [(e), (f)] nonoverlap shells.

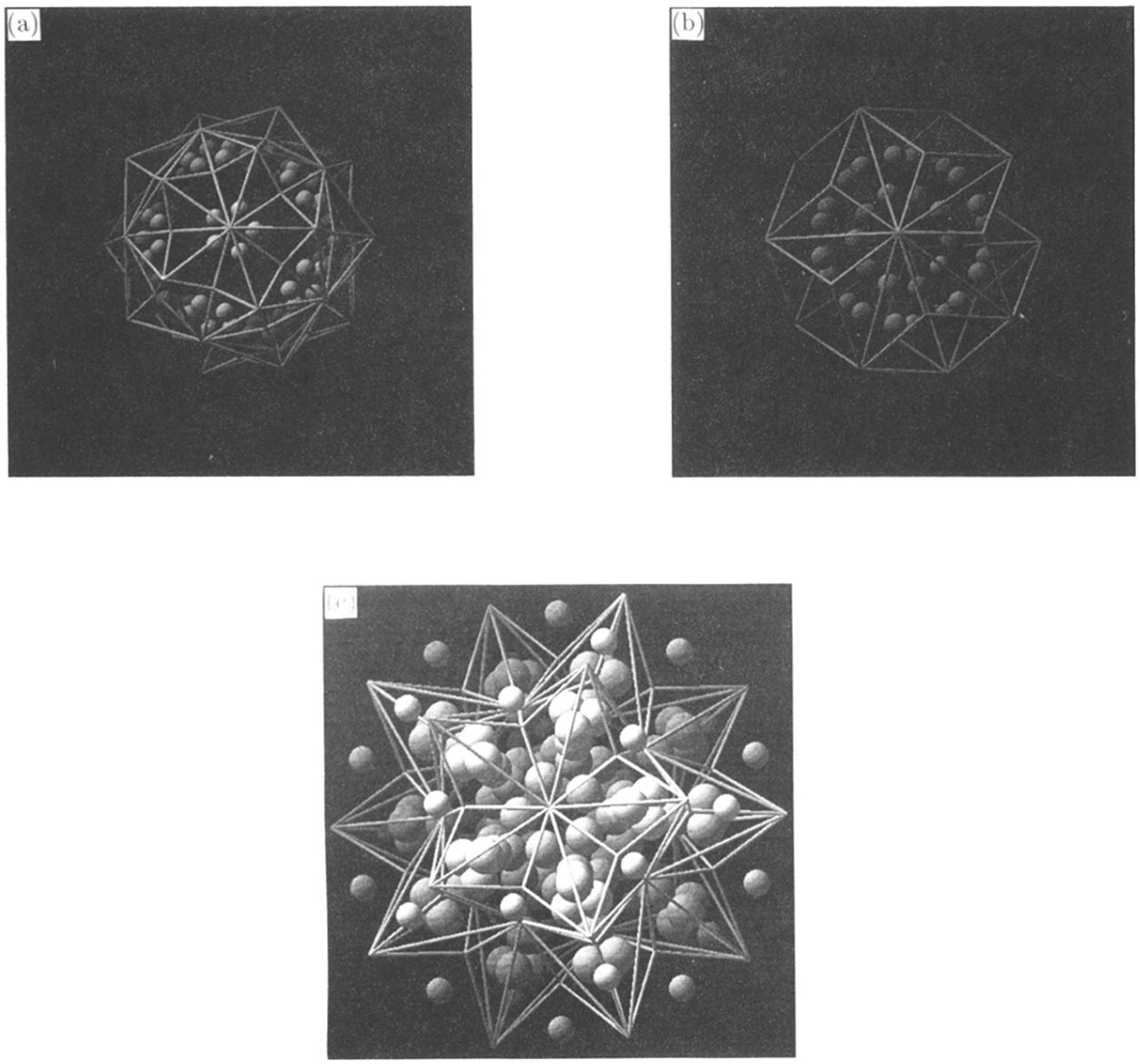

FIG. 4. Ideal inner space locations of the embedded R-$(Al_{0.564}Cu_{0.116}Li_{0.320})$ atoms from Table IV. The clusters of embedded atoms are centered (a) at a vertex for orbit $K=4$, (b) at an edge center for orbits $k=1$ and 5, or (c) at a body center for orbits $k=2$, 3, 6, and 7. The spheres representing Li are the largest, with the size of spheres representing the other embedded atoms decreasing with the increase in Cu fraction. The correct site symmetries result from the five equivalent ways of embedding the crystal symmetry T_h into the hypercrystal symmetry Y_h. We also show the edges of the hyperatoms determined in our model.

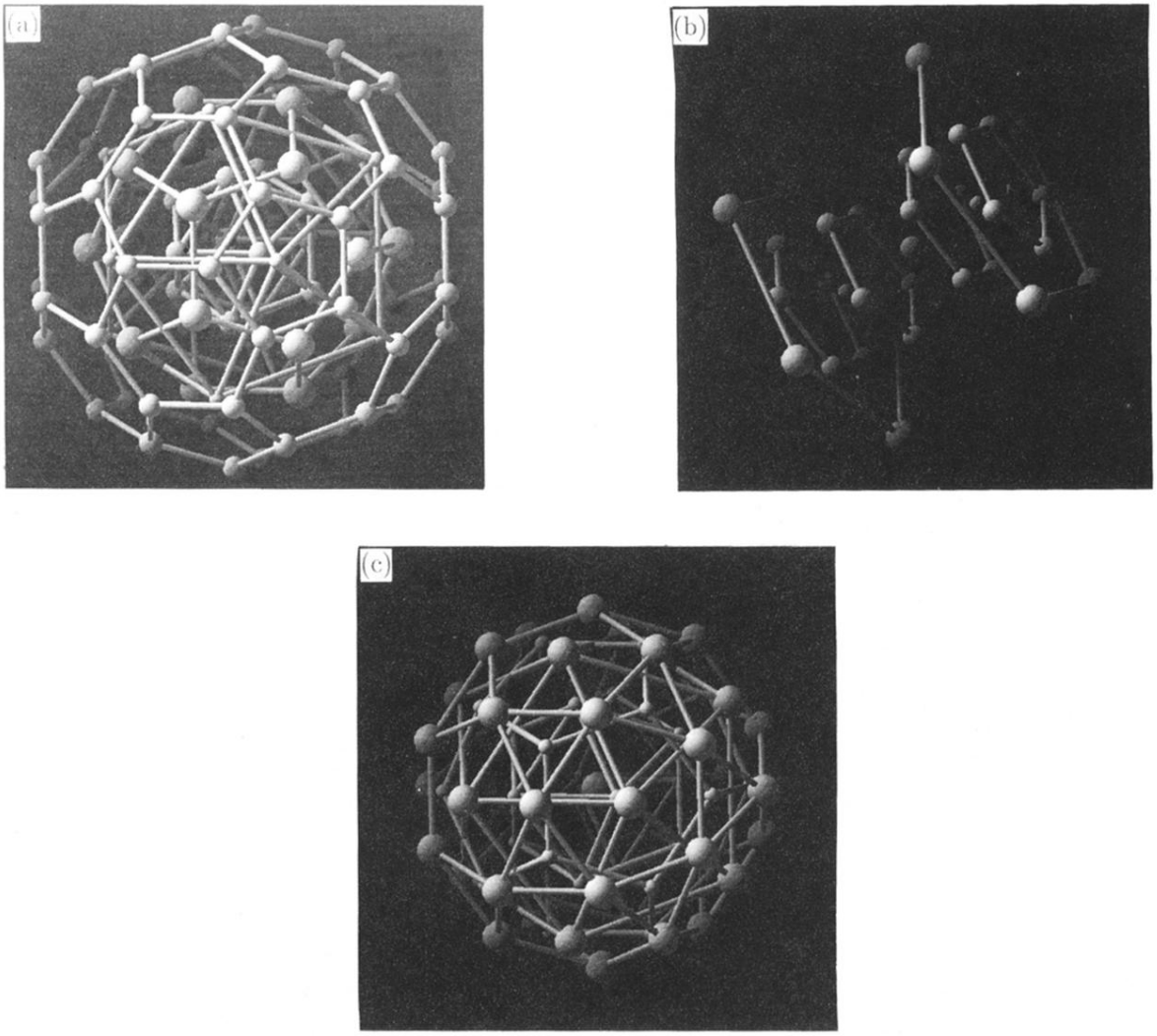

FIG. 6. High-symmetry atomic clusters found for our model in the physical space centered at a (a) vertex, (b) midedge, or (c) a body center of the hypercrystal. All three clusters are shown on the same scale. Atoms originating from V hyperatoms are shown with the smallest spheres, while these from B hyperatoms are shown with the biggest spheres. For clarity, atoms in the same shell are connected.

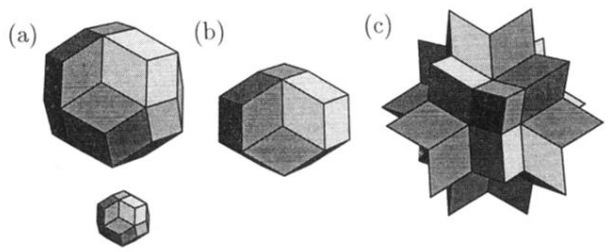

FIG. 8. (a) V, (b) E, and (c) B hyperatoms for the Ammann tiling model of i-$(Al_{0.570}Cu_{0.108}Li_{0.322})$ discussed in Appendix C. The small volume in (a) shows the shape of the hole located at the center of the V hyperatom.

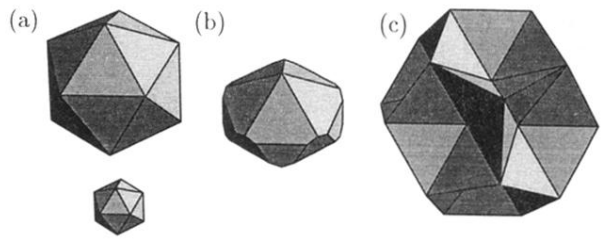

FIG. 9. (a) V, (b) E, and (c) B hyperatoms for the model of i-$(Al_{0.570}Cu_{0.108}Li_{0.322})$ discussed in Appendix D. The small volume in (a) shows the shape of the hole located at the center of the V hyperatom.